Journal Pre-proofs

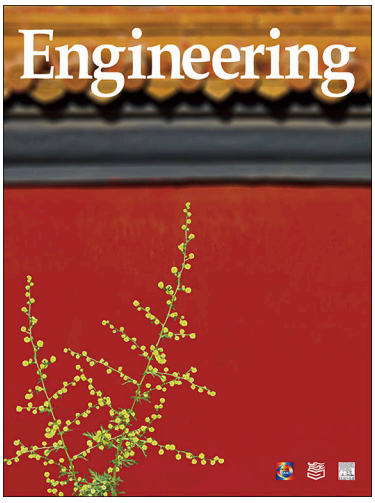

Article

A High-Precision Workpiece Positioning System Based on Super-Resolution Microscopic Vision in Ultra-Precision Machining

Honglu Li, Zhaoyun Li, Bing Wang, Zhanqiang Liu, Muhao Xu, Pengyang Wang

PII: S2095-8099(26)00451-0
DOI: https://doi.org/10.1016/j.eng.2026.07.035
Reference: ENG 2435

To appear in: *Engineering*

Received Date: 30 December 2025
Revised Date: 24 May 2026
Accepted Date: 1 July 2026

Please cite this article as: H. Li, Z. Li, B. Wang, Z. Liu, M. Xu, P. Wang, A High-Precision Workpiece Positioning System Based on Super-Resolution Microscopic Vision in Ultra-Precision Machining, *Engineering* (2026), doi: https://doi.org/10.1016/j.eng.2026.07.035

This is a PDF of an article that has undergone enhancements after acceptance, such as the addition of a cover page and metadata, and formatting for readability. This version will undergo additional copyediting, typesetting and review before it is published in its final form. As such, this version is no longer the Accepted Manuscript, but it is not yet the definitive Version of Record; we are providing this early version to give early visibility of the article. Please note that Elsevier's sharing policy for the Published Journal Article applies to this version, see: https://www.elsevier.com/about/policies-and-standards/sharing#4-published-journal-article. Please also note that, during the production process, errors may be discovered which could affect the content, and all legal disclaimers that apply to the journal pertain.

© 2026 THE AUTHORS. Published by Elsevier LTD on behalf of Chinese Academy of Engineering and Higher Education Press Limited Company

Journal Pre-proofs

Research

Frontiers of Extreme Manufacturing—Article

A High-Precision Workpiece Positioning System Based on Super-Resolution Microscopic Vision in Ultra-Precision Machining

Honglu Li [a,b,c], Zhaoyun Li [d], Bing Wang [a,b,c,*], Zhanqiang Liu [a,c,e], Muhao Xu [a,b,c], Pengyang Wang [f]

[a] *School of Mechanical Engineering, Shandong University, Jinan 250061, China*

[b] *State Key Laboratory of Advanced Equipment and Technology for Metal Forming, Shandong University, Jinan 250061, China*

[c] *Key Laboratory of High Efficiency and Clean Mechanical Manufacture of MOE & Shandong Key Laboratory of High Performance Tools and System, Shandong University, Jinan 250061, China*

[d] *College of Computer Science and Engineering, Jining University, Qufu 273155, China*

[e] *School of Airspace Science and Engineering, Shandong University, Weihai 264209, China*

[f] *Department of Computer and Information Science, University of Macau, Macau 999078, China*

* Corresponding author.

E-mail address: sduwangbing@sdu.edu.cn (B. Wang).

Abstract: Ultra-precision machining generally involves multiple process steps, during which a workpiece needs to be measured offline and re-mounted. Therefore, re-clamping errors apt to cause misalignment of the workpiece between machining stages are inevitable. Even small in-plane rotations and translations can significantly degrade feature alignment and final form accuracy of the machined components during multi-step processes. To address this issue, this paper proposes a high-precision on-machine positioning system based on super-resolution microscopic vision towards accurate measurement of re-clamping errors. Specifically, the system directly uses inherent micro-scale features on the machined surface as intrinsic references to guarantee positioning accuracy. *In-situ* microscopic images are captured before and after re-clamping operation, and then a coarse-to-fine registration pipeline is employed. During the coarse positioning stage, robust geometric feature extraction and geometry constrained fitting can provide a reliable initial three-degree-of-freedom (3-DOF) pose estimate over large rotation and translation ranges. During the fine positioning stage, 3-DOF sub-pixel template matching is performed to accurately estimate the residual positioning error within a small search range. Furthermore, to overcome the resolution limitations of conventional microscopy, a super-resolution reconstruction module tailored to microscopic imaging is used to enhance the effective resolution of microstructure images during fine positioning. Systematic experiments demonstrate that the proposed system can achieve arcsecond-level rotational accuracy over a rotational range of 180° and translational accuracy on the scale of tens of nanometers over a translational range of 180 μm. This proposed approach is a non-contact, high-accuracy, cost-effective, and readily deployable method for practical machining environments, and it has exhibited strong potential for re-clamping pose identification and high-precision workpiece reposition during ultra-precision machining operations.

Keywords: Ultra-precision machining; Clamping errors; Precision positioning measurement; Machine vision; Image registration; Super-resolution reconstruction.

1. Introduction

Ultra-precision machining is a key enabling manufacturing technology widely used in such significate fabrication areas as semiconductor devices, high-performance optical components, and aerospace precision parts [1–3]. Owing to the ability to achieve nanometer-scale surface roughness and sub-micrometer geometric accuracy, ultra-precision machining has become central and indispensable to high-end manufacturing processes [4,5]. As the functional complexity and precision requirements of machined components increase, the measurement of and compensation for machining

Journal Pre-proofs
errors have become an essential research focus [6–8]. In practical industrial applications, many high-value components can no longer be fully manufactured within one single setup. Instead, coordinated multi-process, multi-stage machining methods with associated inspection procedures are required [9,10].

Many representative high-end components need to be manufactured using multiple ultra-precision machining steps [11,12]. A typical case is large aperture reflective mirrors that require off-machine interferometric inspection between cutting steps [13]. Microstructure optical surfaces, such as diffraction gratings and microlens arrays, also demand iterative machining and metrology [14,15]. In addition, high-aspect-ratio microstructure surfaces and microfluidic channel molds often preclude on-machine sensing due to constraints in the working distance, limited numerical apertures, or their underlying measurement principles [16]. These scenarios often require removal of the workpiece from the machine for offline measurement or auxiliary handling, followed by re-clamping of the workpiece for secondary machining. However, this removal and re-installation inevitably introduce re-clamping errors [12,17]. Even small in-plane translations or rotations during the re-clamping process can cause systematic misalignment between the toolpath expressed in the original coordinate frame and the actual workpiece pose [18]. The consequences of such misalignment include misregistration between sequential features, overlap or gaps at stitched regions, and accumulated profile errors in the machined components [14,19]. This effect is particularly severe for dense and fine microstructures in which the feature spacing is small and the tolerance margins are extremely limited [20-22]. Therefore, after re-clamping has been performed, a positioning system with high-accuracy and high repeatability must be used to reconstruct the original coordinate frame and enable reliable compensation.

In practice, workpiece positioning during re-clamping is typically achieved using dedicated fixtures and mechanical datum transfer [23,24]. However, the accuracy of this method is inherently constrained by manufacturing tolerances, assembly errors, wear, and micro-elastic deformation that are induced by the clamping forces. Such factors render the fixture accuracy unable to stably reach the micrometer level [25,26]. High-end *in-situ* positioning systems equipped with laser interferometry can deliver excellent accuracy. However, they typically require multiple interferometer channels, carefully prepared planar mirror references on the workpiece, and substantial system costs that limit their general applicability [27–29]. Deflectometry-based methods of positioning mirror-like workpieces have the potential to simplify the system architecture to some extent. Nevertheless, their applicability is limited because their achievable accuracy typically remains at the micrometer level, which is insufficient for ultra-precision machining applications [30,31].

Microscopic vision is a promising tool for precision positioning because it directly captures micro-scale surface features and infers pose deviations using image registration [32–34]. Existing vision-based positioning methods for machining applications generally include image acquisition, pre-processing, feature extraction, and target localization. These methods can be broadly classified as feature-based, template matching-based, or learning-based approaches [35]. Feature-based methods, which rely on edges, corners, or hand-crafted descriptors, offer clear physical interpretability at relatively low computational costs. However, their robustness is often limited by illumination variations, repetitive textures, and weak local distinctiveness, especially when they are used for microscopic images of machined surfaces. Template matching-based methods estimate pose by evaluating the similarity between a reference template and a target region. These methods enable more effective use of contour and grayscale information. However, their computational costs increase rapidly with the search range and the number of degrees of freedom. In addition, their robustness may deteriorate in the presence of large rotations, partial overlap, or image degradation. Learning-based methods, particularly deep-learning-based detection and registration approaches, have strong representation capabilities and improved robustness when used in complex scenarios. Nevertheless, they typically require large task-specific datasets and substantial training resources, and their metrological interpretability and generalization remain inadequate for ultra-precision machining applications. During ultra-precision machining operations, surface topography variations produce distinctive intensity responses in reflection-based microscopy [36]. Sharp changes at microstructure boundaries lead to pronounced intensity transitions that support stable geometric-feature extraction, while the interior regions of grooves generally exhibit continuous grayscale distributions that are well suited for intensity consistency-based registration [37,38]. Despite these advantages, the use of conventional vision-based alignment in ultra-precision scenarios faces two main obstacles. Firstly, the effective resolution of standard microscopy is limited by optical diffraction, sensor sampling, and

Journal Pre-proofs
noise. Consequently, a single pixel may correspond to hundreds of nanometers on the workpiece, and such resolution is insufficient for nanometer-scale positioning [39–41]. Secondly, images captured before and after re-clamping may exhibit large initial translations and in-plane rotations, partial non-overlap, and limited reliable texture, which makes robust registration challenging [42,43]. Therefore, a practical solution must provide a large capture range as well as ultra-high precision, and it must remain reliable under practical machining conditions.

In view of the considerations presented above, a high-precision workpiece positioning system that is based on super-resolution microscopic vision was developed during this study, with the goal of obtaining accurate identification and high-precision positioning of re-clamping-induced errors. The system, which can be modularly integrated into an ultra-precision machine tool, treats the machined microstructure as an intrinsic reference pattern and measures the three-degree-of-freedom (3-DOF) pose deviation of the workpiece by means of image registration. To address the limited effective resolution associated with microscopic images, a deep-learning-based super-resolution reconstruction model was developed by combining a local implicit image function (LIIF) formulation with a residual dense network (RDN) encoder [44,45]. The proposed model enables continuous-scale reconstruction of microstructure images and thereby effectively enhances the effective resolution of microscopic imaging. In addition, a dataset construction method that is suitable for microscopic super-resolution reconstruction was developed, and a dedicated super-resolution dataset for ultra-precision machined microstructure images was established to support model training and performance evaluation. To balance the measurement range, positioning accuracy, and computational efficiency, a hierarchical registration framework that consists of three sequential stages including coarse positioning, super-resolution reconstruction, and fine positioning was further proposed. During the coarse positioning stage, a geometry constraint method is used to achieve rapid and robust initial estimations under relatively large pose deviations [46]. In the super-resolution reconstruction stage, the effective resolution of the microscopic images and the distinguishability of fine details are enhanced. In the fine positioning stage, a template matching-based method is used to achieve high-precision estimations of the residual pose deviations.

Comprehensive machining and measurement experiments were performed to validate the system performance. Imaging stability tests confirmed that the on-machine microscope could capture consistent microstructure images under practical machining conditions. Coarse positioning experiments demonstrated reliable initialization across wide motion ranges, which included a rotation span of 180° and a translation stroke of 180 μm, with concentrated errors and no evident drift. Super-resolution experiments showed that the proposed dataset and the RDN-LIIF model effectively enhanced the microscopic image resolution and improved the subsequent registration accuracy. Fine positioning experiments further demonstrated arcsecond-level rotation estimations and a translation measurement capability on the order of tens of nanometers. In addition, system-level experiments verified the accuracy, efficiency, and engineering feasibility of the proposed positioning system.

Overall, the proposed super-resolution microscopic vision-based positioning system provides an effective, non-contact solution for the measurement of re-clamping errors during ultra-precision manufacturing. Future work will extend the framework to higher-degree-of-freedom and broader precision positioning applications while simultaneously improving the system robustness in the presence of more challenging operating conditions.

2. Re-clamping error analysis and positioning system conception

2.1. Analysis of workpiece re-clamping issues

In the machining scenario that was considered during this study, re-clamping primarily causes in-plane pose change of the workpiece, while height variations are negligible. Therefore, the re-clamping error can be simplified into a two-dimensional (2D) rigid-body transformation with translation and rotation components. For this analysis, (x, y) denote the coordinates of an arbitrary point on the workpiece in the initial clamping state, while (x', y') represent the corresponding coordinates in the machine coordinate frame after re-clamping has been performed. This relationship is described by Eq. (1).

$$\begin{bmatrix} x \\ y' \end{bmatrix} = \boldsymbol{R}(\Delta\theta)\begin{bmatrix} x \\ y \end{bmatrix} + \begin{bmatrix} \Delta x \\ \Delta y \end{bmatrix} \tag{1}$$

where $\Delta\theta$ represents the rotational-error angle of the workpiece about the axis perpendicular to the machining plane, while Δx and Δy represent the in-plane translational errors in the x- and y-directions, respectively. $\boldsymbol{R}(\cdot)$ represents the 2D rotation matrix.

The rigid-body pose deviation misaligns the workpiece coordinate frame with respect to the original machining frame, and this misalignment produces a systematic offset between the planned toolpath and the actual workpiece location. When there is no compensation, the re-clamping error would directly map to the machining result while significantly degrading the multi-step feature alignment and final form accuracy. Therefore, accurate identification of and compensation for this error are critical prerequisites to the achievement of high-precision secondary machining.

To achieve high-precision identification of and compensation for re-clamping errors, a microscopic vision-based positioning method was adopted during this study. It is physically based on the inherent mapping between the surface topography and the pixel-intensity distribution in the microscopic imaging process [47]. In a typical reflection-based microimaging setup, uniform illumination is projected onto the machined microstructure. The reflected light is collected by an objective lens and relayed through the imaging optics, and the camera samples the continuous irradiance field into a discrete digital image [36,48]. Fig. 1 depicts the optical imaging process for an ultra-precision machined microgroove array, as well as the pixel-intensity distribution characteristics of its image. This imaging process can be divided into three stages: surface reflection, optical imaging, and camera sampling. From a physically grounded perspective, the reflected radiance can be described by a bidirectional reflectance distribution function $f_r(\cdot)$, which describes how incident light is redistributed by the surface into various outgoing directions. For a surface point x, the outgoing radiance ($L_o(\cdot)$) in direction $\boldsymbol{\omega}_o$ can be described with Eq. (2).

$$L_o(\boldsymbol{\omega}_o) = \int_{\Omega^+} f_r(\boldsymbol{\omega}_i, \boldsymbol{\omega}_o) L_i(\boldsymbol{\omega}_i) \cos\theta_i \, d\boldsymbol{\omega}_i \tag{2}$$

where $L_i(\cdot)$ represents the incident radiance, $\boldsymbol{\omega}_o$ and $\boldsymbol{\omega}_i$ are the incident and outgoing directions, respectively, Ω^+ represents the hemisphere of incident directions above the surface, and θ_i denotes the incident angle.

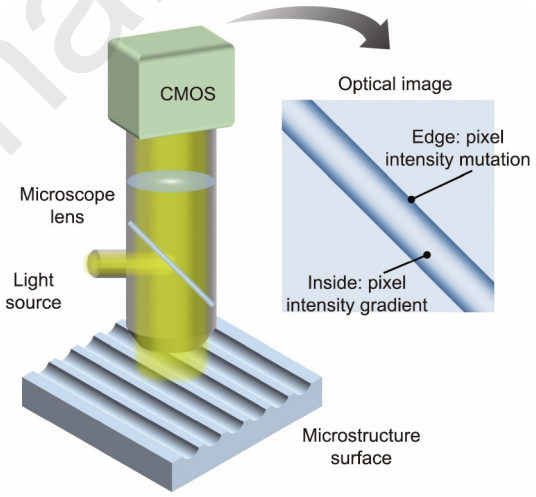

Fig. 1. Optical imaging process of ultra-precision machined microstructure surface and associated pixel intensity distribution of captured image.

After it passes through the optical system, the outgoing radiance field forms a continuous luminance distribution on the image plane under incoherent illumination. This process is commonly modeled as a convolution in which the system point-spread function can be expressed with Eq. (3).

$$E(\boldsymbol{u}) = \int L_o(\boldsymbol{x}) h(\boldsymbol{u} - M\boldsymbol{x}) \mathrm{d}\boldsymbol{x} \tag{3}$$

where $E(\boldsymbol{u})$ represents the continuous image-plane intensity, M denotes the magnification, and $\boldsymbol{u}$ represents the spatial coordinate on the image plane. $h(\cdot)$ is the point spread function, which describes the spatial spreading of light from an ideal point source that is caused by diffraction and optical aberrations.

Finally, the camera integrates $E(\boldsymbol{u})$ over each pixel area $\Omega_{m,n}$ to obtain the discrete grayscale value. This process can be expressed with Eq. (4).

$$I_{m,n} = \eta \int_{\Omega_{m,n}} E(\boldsymbol{u}) \mathrm{d}\boldsymbol{u} \tag{4}$$

where η represents the photoelectric conversion gain.

When the normal surface of the workpiece profile is close to the illumination and imaging optical axis, the reflected light can be effectively coupled into the objective lens, which results in higher pixel intensities in the corresponding image regions. When the local surface is tilted, the reflected light deviates from the imaging optical path, which leads to a significant decrease in the pixel intensity. Fig. 1 shows that, in the microgroove boundary regions, abrupt surface topography changes cause drastic variations in the local surface normal orientation, which in turn lead to rapid changes in the reflection conditions. These changes are manifested in the microscopic images as pronounced pixel intensity mutations, which correspond to clear edge responses. In contrast, within the interior regions of the microgroove, the surface height and slope typically vary continuously. Thus, the corresponding pixel-intensity distribution exhibits smooth and gradually varying characteristics.

The intensity distribution characteristics that are observed in these different regions provide a physical basis for the image registration strategy. The intensity discontinuities at the microgroove boundaries offer high contrast and stable spatial localization, which cause them to be suitable for geometric feature extraction and geometry constraint based feature registration. Meanwhile, the continuously varying pixel intensity distributions inside the grooves contain rich grayscale information, which is ideal for use in intensity consistency-based image registration methods that are used to achieve sub-pixel-level fine pose estimations. Therefore, within a unified microscopic vision framework, the complementary advantages of geometric features and grayscale information can be fully exploited for coarse positioning and fine positioning, respectively. Therefore, the overall positioning accuracy and robustness can be significantly improved.

2.2. Conception of workpiece positioning system

According to the principles that were described above, a complete ultra-precision machining workpiece positioning system that is based on super-resolution microscopic vision was established during this study. The detailed procedure followed by this system is illustrated in Fig. 2. Through the close cooperation of multiple modules, the system forms an integrated pipeline for 3-DOF positioning and compensation of a workpiece. Its goal is the accurate identification of and compensation for re-clamping errors.

Journal Pre-proofs

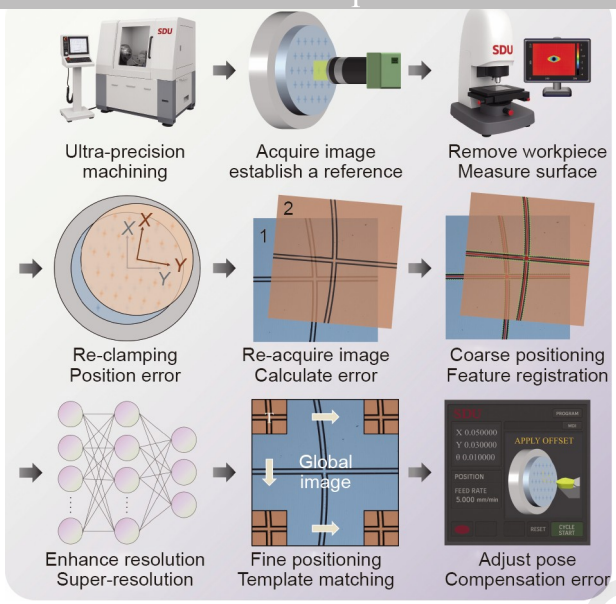

Fig. 2. Conception of workpiece positioning system based on super-resolution microscopic vision towards ultra-precision machining process.

After the initial machining step, the microstructure surface is imaged *in-situ* using the on-machine microscopic vision system, which obtains a reference image and defines the reference coordinate frame. The workpiece is then removed for off-machine inspection or intermediate operations and is subsequently re-clamped for the next machining step. After the re-clamping process, the same region is re-imaged in order to acquire the target image for registration. During the re-imaging process, the camera pose and illumination are maintained the same as they were during the reference acquisition process to ensure image comparability. A coarse-to-fine hierarchical registration strategy is used to simultaneously achieve robustness and precision. Specifically, a feature-based module first provides a reliable initial pose estimate to constrain the search space. A deep-learning-based super-resolution reconstruction module is then employed to enhance the effective resolution of the microscopic image. In addition, an intensity-based registration module performs refined 3-DOF alignment within the constrained neighborhood, thereby enabling accurate estimation of the re-clamping-induced pose deviation. Finally, the resulting pose deviation is then compensated for either by inverse motion of the positioning stage or by equivalent coordinate offsets in the numerical control program.

3. Image processing algorithms for high-precision positioning

During this study, a hierarchical coarse-to-fine image registration framework that consists of three sequential stages including coarse positioning, super-resolution reconstruction, and fine positioning was employed. Firstly, the coarse positioning stage provides a robust initial estimate of the in-plane pose deviation under conditions with relatively large translations and rotations. Thus, the subsequent search range is effectively constrained. Next, super-resolution reconstruction is conducted to enhance the effective resolution of the microscopic images and improve the distinguishability of the fine structural details. Finally, fine positioning is performed within a constrained local neighborhood to achieve high-precision estimation of the residual pose deviation.

3.1. Coarse positioning based on geometric constraints

In re-clamping operations for ultra-precision machining processes, the images that are acquired after re-clamping generally exhibit large translations and in-plane rotations, partial non-overlap, and limited reliable texture with respect to the initial images. To obtain a robust initial estimate, the coarse positioning was formulated as a geometric constraint problem during this study. This method exploits repeatedly detectable geometric primitives, such as lines and curves [49]. By integrating sub-pixel edge extraction with geometric fitting, a rapid 3-DOF pose estimation can be achieved [50]. Fig. 3 illustrates the schematic workflow of the proposed coarse positioning method.

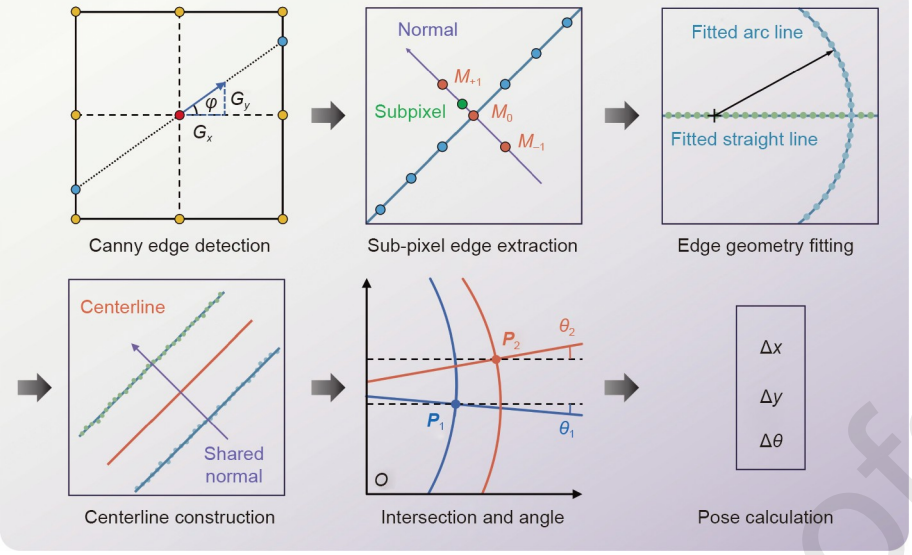

Fig. 3. Flowchart of coarse positioning algorithm based on geometric constraints. $\boldsymbol{P}_1$, $\boldsymbol{P}_2$: coordinates vectors of the microstructure intersection point before and after re-clamping, respectively; θ_1, θ_2: orientation angles of the groove centerline before and after re-clamping, respectively.

Firstly, Canny edge detection is used to extract pixel points along the microgroove boundaries [37]. The gradient magnitude and orientation of each pixel can be obtained with Eqs. (5) and (6).

$$\begin{cases} G_x = \partial I_s / \partial x \\ G_y = \partial I_s / \partial y \end{cases} \tag{5}$$

$$\begin{cases} M(x,y) = \sqrt{G_x^2 + G_y^2} \\ \varphi(x,y) = \arctan\left(G_y / G_x\right) \end{cases} \tag{6}$$

where M denotes the gradient magnitude, and φ denotes the gradient direction. After non-maximum suppression and double-threshold hysteresis linking are performed, a pixel-level edge set, $\Omega = \boldsymbol{q}_i$, can be obtained. I_s denotes the pixel intensity of the smoothed grayscale image; G_x and G_y denote the image gradient components in the x- and y-directions, respectively.

Then, each pixel-level edge point, $\boldsymbol{q}_i$, is refined to a sub-pixel location by performing three-point quadratic interpolation along the normal direction of the gradient. The unit normal vector, $\boldsymbol{n}_i$, at $\boldsymbol{q}_i$ is given by Eq. (7).

$$\boldsymbol{n}_i = \frac{1}{M(\boldsymbol{q}_i)} \begin{bmatrix} G_x(\boldsymbol{q}_i) \\ G_y(\boldsymbol{q}_i) \end{bmatrix} \tag{7}$$

Three samples are taken along the gradient normal direction (M_{-1}, M_0, and M_{+1}), as expressed in Eq. (8).

$$M_{-1} = M(\boldsymbol{q}_i - \boldsymbol{n}_i), \quad M_0 = M(\boldsymbol{q}_i), \quad M_{+1} = M(\boldsymbol{q}_i + \boldsymbol{n}_i) \tag{8}$$

The sub-pixel offset, s^*, is obtained by conducting quadratic interpolation, as shown in Eq. (9).

$$s^* = \frac{M_{-1} - M_{+1}}{2\left(M_{-1} - 2M_0 + M_{+1}\right)} \tag{9}$$

Journal Pre-proofs

Accordingly, the sub-pixel edge point set, $\boldsymbol{x}_i$, can be obtained from Eq. (10):

$$\boldsymbol{x}_i = \boldsymbol{q}_i + s_i \boldsymbol{n}_i \tag{10}$$

Next, the sub-pixel edge points are classified according to the microstructure type and are fitted with corresponding geometric models. For example, the edge point set is fitted using least-squares line fitting for straight grooves. Similarly, the circle parameters are obtained by fitting a circle to the edge points, which is accomplished by minimizing the radial residuals for the arc grooves. In this way, parametric equations for the edges of each microstructure in the image can be determined [51].

The groove centerlines are subsequently constructed using the two opposing edges of each groove. For a straight groove, the centerline is given by the bisector of the two fitted edge lines. If the fitting results of the two edges are denoted as ($\boldsymbol{n}_\mathrm{L}$, $\rho_{\mathrm{L}1}$) and ($\boldsymbol{n}_\mathrm{L}$, $\rho_{\mathrm{L}2}$), then the straight-groove centerline can be expressed by Eq. (11).

$$\boldsymbol{n}_\mathrm{L}^\mathrm{T} \boldsymbol{x} - \rho_{\mathrm{Lc}} = 0, \quad \rho_{\mathrm{Lc}} = \frac{\rho_{\mathrm{L}1} + \rho_{\mathrm{L}2}}{2} \tag{11}$$

For an arc groove, the centerline is constructed as a concentric circle whose radius is equal to the mean of the radii of the two fitted edge circles. If the two edge circles are fitted as (u_1, v_1, R_1) and (u_2, v_2, R_2), then the parameters of the arc-groove centerline can be obtained from Eq. (12).

$$u_\mathrm{c} = \frac{u_1 + u_2}{2}, \quad v_\mathrm{c} = \frac{v_1 + v_2}{2}, \quad R_\mathrm{c} = \frac{R_1 + R_2}{2} \tag{12}$$

where (u_i, v_i) denotes the circle center, and R_i denotes the circle radius.

Subsequently, the orientation angle and the intersection points of the centerlines are computed. For a straight-groove centerline, if $\boldsymbol{n}_\mathrm{L} = [n_x, n_y]^\mathrm{T}$, then its direction vector and orientation angle are given by Eq. (13).

$$\boldsymbol{t}_\mathrm{L} = \begin{bmatrix} -n_y \\ n_x \end{bmatrix}, \quad \theta = \mathrm{atan2}(n_x, -n_y) \tag{13}$$

Using the parametric equations for the centerlines, the coordinate vector, $\boldsymbol{P}$, of the microstructure intersection point can be solved. Since the intersection point is clear and unique, a unique solution can be obtained by restricting the calculations within a region of interest. Accordingly, the orientation angles, θ_1 and θ_2, as well as the coordinate vectors of the intersection point, $\boldsymbol{P}_1$ and $\boldsymbol{P}_2$, can be obtained for the image frames that were acquired before and after re-clamping, respectively.

Finally, the positioning result is derived from the intersection point and the orientation information. The rotation angle is defined as the difference between the orientation angles of the two images, and it can be obtained with Eq. (14).

$$\Delta\theta = \mathrm{wrap}(\theta_2 - \theta_1) \tag{14}$$

where wrap(·) maps the angle into the interval (−π, π].

Because the intersection point corresponds to the same physical feature both before and after re-clamping, its displacement reflects the overall translation of the workpiece. While taking the intersection point as a stable reference, the translation vector, $\Delta\boldsymbol{t}$ can be calculated with Eq. (15).

$$\Delta\boldsymbol{t} = \boldsymbol{P}_2 - \boldsymbol{R}(\Delta\theta)\boldsymbol{P}_1 \tag{15}$$

Although coarse positioning can provide a reliable initial estimate over a relatively large search range, its measurement accuracy remains limited by the effective resolution of the original

Journal Pre-proofs

microscopic images. Therefore, super-resolution reconstruction is performed after the coarse positioning process to improve the effective image resolution for the subsequent fine positioning.

3.2. Super-resolution reconstruction of microstructure images

During the microscopic imaging process, optical diffraction, discrete sensor sampling, and electronic readout noise all limit the effective resolution of microstructure images. Consequently, conventional optical microscopy typically remains at the sub-micrometer level in effective resolution, which is insufficient for the nanometer-level positioning required by ultra-precision machining processes. To address this limitation, an image super-resolution reconstruction module is utilized prior to the fine positioning process. This module can recover high-resolution details from low-resolution observations and compensate for the loss of high-frequency information during imaging.

Super-resolution is an ill-posed up-sampling inverse problem in which a single low-resolution pixel may correspond to multiple high-resolution interpretations [52]. Deep learning-based super-resolution methods have achieved notable advances in both resolution enhancement and detail fidelity. Therefore, such methods have become the dominant technical route [53]. Although numerous public super-resolution datasets for natural macroscopic scenarios are available, their texture statistics, illumination conditions, dynamic ranges, and noise characteristics differ substantially from those of microstructure microscopy applications [54]. This discrepancy hinders the direct application of generic models that have been trained on natural images and that may induce biased edge profiles or non-physical pseudo-details, which degrade the reliability of subsequent registration and metrology [55].

Therefore, a dedicated microstructure super-resolution reconstruction dataset that is tailored to microscopic imaging was developed during this study [56]. As shown in Fig. 4, high-resolution images of diverse microstructures were acquired using a laser confocal microscope. The laser confocal microscope performed optical sectioning via point scanning and pinhole-based confocal detection, which effectively suppresses out-of-focus stray light and reduces the effective point spread function. Therefore, images with higher fidelity than those obtained by conventional optical microscopes were obtained with this method. In addition, to further improve the generalization capability and robustness of the model, multi-dimensional parameter perturbations and scenario coverage were utilized during the dataset construction. The dataset covers various workpiece materials, tool geometries, and cutting-parameter combinations, as well as a variety of machined features, such as single grooves, intersecting grooves, and continuous grooves. Meanwhile, microscopic images that were acquired under various illumination intensities were also captured. The constructed dataset consists of 807 images, of which 707 were allocated to the training set and 100 to the validation set.

Given the distinct characteristics of microstructure microscopic images and the challenges associated with data acquisition, the LIIF model, which is capable of super-resolution at arbitrary scales, was employed. Unlike methods that utilize fixed super-resolution factors, LIIF models a continuous image as a collection of latent code sets that are distributed within a 2D space. The decoding function uses a query coordinate and its neighboring latent codes as input. Afterwards, it directly predicts the red–green–blue (RGB) value that corresponds to that coordinate. By leveraging coordinate continuity, this representation supports image reconstruction and generation at arbitrary resolutions.

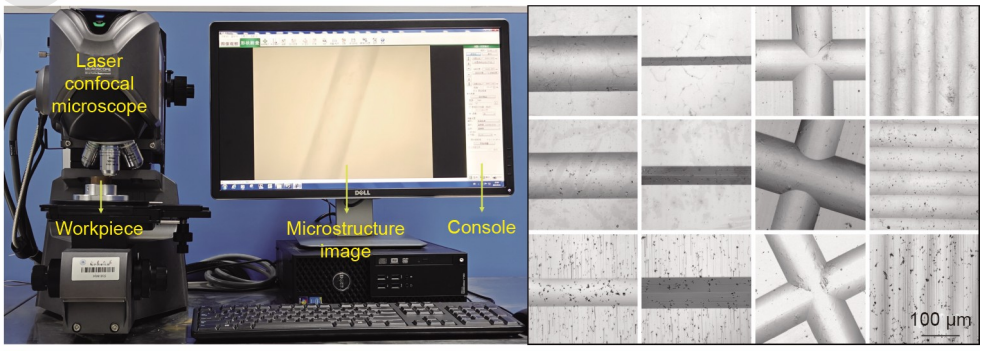

(a) (b)

Journal Pre-proofs

Fig. 4. Construction of the high-resolution microstructure image dataset: (a) Laser confocal microscope used for image acquisition; (b) samples of high-resolution microstructure images.

The overall architecture of LIIF is illustrated in Fig. 5. Fig. 5(a) depicts the data processing procedure. To optimize model training, high-resolution images are subjected to random cropping and down-sampling in order to generate pairs of high- and low-resolution image patches, after which data augmentation is performed. These image patches, which are tailored for the implicit neural representation network architecture, are converted into sets of coordinate–RGB pairs. To help the model perceive pixel coverage ranges at various scales, the normalized pixel cell size that corresponds to each query coordinate is also calculated.

The specific LIIF implementation workflow is presented in Fig. 5(b). For a given low-resolution input image I_{LR}, an encoder first extracts a 2D feature map $\boldsymbol{M} \in ¡^{H \times W \times D}$, where D represents the number of feature channels. Unlike traditional super-resolution methods that directly up-sample feature maps, this LIIF method treats the image as a function that is defined over a continuous 2D domain $\boldsymbol{\Omega}$.

The objective for any query coordinate $\boldsymbol{x}_q \in \boldsymbol{\Omega}$ within the continuous domain is to predict its corresponding RGB signal $\boldsymbol{s}(\boldsymbol{x}_q)$. The LIIF method models this prediction process as an implicit mapping function f_θ, which is based on local features and is parameterized by a multi-layer perceptron (MLP). The fundamental prediction formula is defined with Eq. (16).

$$\boldsymbol{s}(\boldsymbol{x}_q) = f_\theta\left(\boldsymbol{z}^*, \boldsymbol{x}_q - \boldsymbol{v}^*, \boldsymbol{c}\right) \tag{16}$$

where $\boldsymbol{z}^*$ denotes the feature vector (latent code) in the feature map that is nearest to $\boldsymbol{x}_q$, and $\boldsymbol{v}^*$ represents the center coordinate that corresponds to $\boldsymbol{z}^*$ in the image domain. The term $\boldsymbol{x}_q - \boldsymbol{v}^*$ represents the relative coordinate, which indicates the offset of the query point relative to the local feature center. This term is critical to the achievement of continuous resolution because it enables f_θ to learn the local texture variations of the same feature at different relative positions. In addition, $\boldsymbol{c}$ represents the cell decoding information, which contains the height and width of the query pixel at the target resolution. It can be used to help the network eliminate aliasing effects that are induced by scale variations.

Journal Pre-proofs

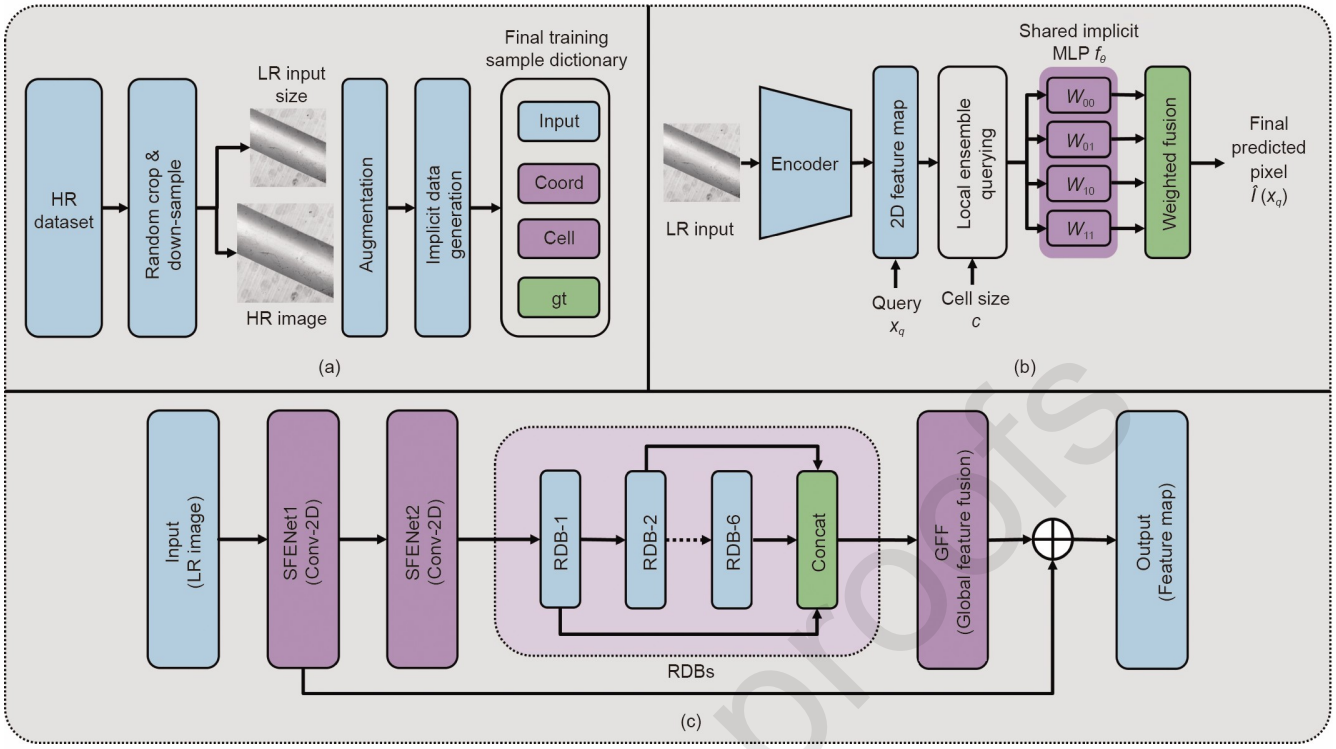

Fig. 5. Overview of LIIF algorithm used in this research. LR: low resolution; Conv: convolutional layer; HR: high resolution; gt: ground-truth image.

To enrich the contextual information of local features, a feature unfolding mechanism was developed. During the extraction of z^*, rather than utilizing a single point feature at v^*, the features within its 3 × 3 neighborhood are concatenated with Eq. (17).

$$z^* = \mathrm{Concat}\left(\left\{ M_{v^*+\delta} \mid \delta \in \{-1,0,1\}^2 \right\}\right) \tag{17}$$

Consequently, the feature dimension input to f_θ is expanded to nine dimensions, and this expansion significantly enhances the ability of the model to capture local structural relationships.

Next, the nearest neighbor feature is directly employed to obtain prediction results in discontinuous artificial artifacts at the boundaries of the feature grid in the generated image. To address this issue, a local ensemble strategy, which was inspired by bilinear interpolation but is utilized at the level of prediction values, was developed. For any x_q, the set of the four nearest feature centers, $V = \{v_{00}, v_{01}, v_{10}, v_{11}\}$ (which correspond to the top-left, top-right, bottom-left, and bottom-right neighboring features, respectively), is selected. The model performs an independent prediction for each feature center in the set as Eq. (18).

$$\hat{s}_t = f_\theta\left(z_t, x_q - v_t, c\right) \tag{18}$$

where z_t and v_t are the feature vector and the corresponding coordinate, respectively, after the feature unfolding mechanism has been applied. The final predicted value $\hat{I}(x_q)$ is the weighted sum of these four independent predictions, as shown by Eq. (19).

$$\hat{I}\left(x_q\right)=\sum_{t\in\{00,01,10,11\}}\frac{W_t}{W}\cdot\hat{s}_t \tag{19}$$

where W denotes the total area of the rectangle that is enclosed by the four feature centers. The calculation of the weight W_t follows the diagonal area rule (which is consistent with bilinear interpolation logic). Specifically, the weight of z_t is proportional to the area of the rectangle that is formed by x_q and the feature center coordinate $v_{t'}$ diagonally opposite to v_t. By means of this local ensemble mechanism, the LIIF method achieves smooth transitions between the feature grids, thereby ensuring the spatial continuity of the generated image at any continuous coordinate.

The encoder employs the RDN architecture, as shown in Fig. 5(c). The RDN was designed to fully utilize the hierarchical features of the image, and its overall architecture consists of three parts: shallow feature extraction (SFENet), stacked residual dense blocks (RDB), and global feature fusion (GFF). The input image first passes through a two-layer convolutional network for the extraction of shallow features. The output feature map of the first layer not only serves as the input for subsequent deep networks but also directly participates in the final global residual connection. With the aid of super-resolution reconstruction, the microstructure images retain richer grayscale and structural details at an enhanced effective resolution, thereby providing more favorable input for the high-precision image registration.

3.3. Fine positioning based on image intensity

Based on the coarse positioning result and the super-resolved images, fine positioning is further performed within the constrained local search range to more accurately estimate the residual pose deviation. Under such a reduced search space, intensity-based registration becomes more advantageous because it can directly exploit the continuous and distinguishable grayscale distribution within the groove to achieve high-precision localization. Accordingly, a high-accuracy 3-DOF registration is performed by maximizing the grayscale intensity consistency in the microscopic images during the fine positioning stage, thereby enabling a refined pose estimation.

Unlike conventional template matching only searching translations, the proposed fine positioning method explicitly incorporates in-plane rotation as a search variable, thereby forming a 3-DOF template matching framework [57,58]. This framework improves the rotation estimation and reduces the disparity caused by residual angular misalignment. Fig. 6 illustrates the workflow of the fine positioning stage, which is based on 3-DOF sub-pixel template matching.

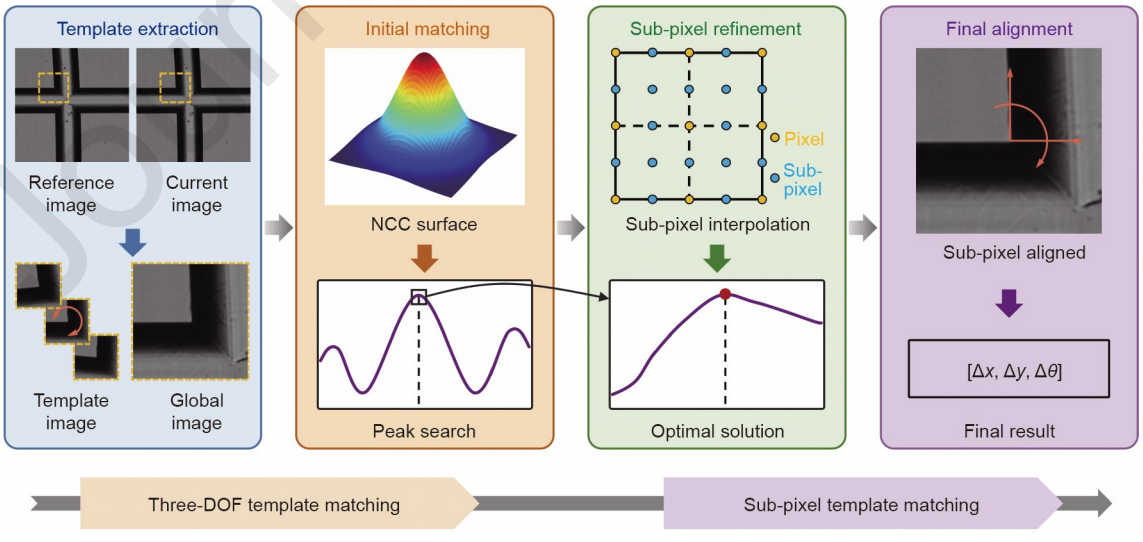

Fig. 6. Flowchart of fine positioning algorithm based on 3-DOF sub-pixel template matching.

Journal Pre-proofs

Firstly, the reference image I_r acquired during the first imaging step is used to construct the template. A template region of interest is then extracted from this template, as shown in Eq. (20).

$$T(\boldsymbol{x}) = I_{\mathrm{r}}(\boldsymbol{x}), \quad \boldsymbol{x} \in \Omega_{\mathrm{T}} \tag{20}$$

where Ω_{T} denotes the template region. The image acquired during the second capture is treated as the current image I_c. The region of interest surrounds the microgroove intersection, where rich pixel intensity variations are present, thereby ensuring matching accuracy and reliability. According to the coarse positioning result, a search window Ω_{S} is defined on I_{C} to avoid the computational explosion and potential disparity that are associated with global searching.

The template is sampled in rotation around the coarse-estimated initial angle, $\Delta\theta_0$. Within the rotation-error range given by the coarse positioning process, discrete candidate angles are generated according to Eq. (21).

$$\theta_k = \Delta\theta_0 + k \cdot \Delta\theta_{\mathrm{s}}, \quad k = -K, ..., K \tag{21}$$

where $\Delta\theta_s$ represents the angular step size, K represents the maximum number of angular search steps on either side of the initial angle. For each candidate angle θ_k, a rotated template is produced by interpolation according to Eq. (22).

$$T_{\theta_k}(\boldsymbol{x}) = T\left(\boldsymbol{R}(-\theta_k)(\boldsymbol{x} - \boldsymbol{a}) + \boldsymbol{a}\right) \tag{22}$$

where $\boldsymbol{a}$ is the template center, and $\boldsymbol{R}(\cdot)$ denotes the 2D rotation matrix. Inverse mapping (θ_k) is used with the intention of preventing holes after rotation and of ensuring that each output pixel can be obtained by means of continuous sampling from the original template. Bicubic interpolation is utilized to reduce re-sampling errors.

Then, for each θ_k, the optimal translation (u, v) is searched within Ω_{S} such that the template best matches the local patch of the current image. The candidate patch in the current image shifted by (u, v) is defined as Eq. (23).

$$P_{u,v}(\boldsymbol{x}) = I_{\mathrm{C}}\left(\boldsymbol{x} + [u, v]^{\mathrm{T}}\right), \quad \boldsymbol{x} \in \Omega_{\mathrm{T}} \tag{23}$$

The normalized cross-correlation (NCC), which is used as the similarity metric, can be expressed as Eq. (24).

$$\mathrm{NCC}(u, v, \theta_k) = \frac{\sum_{\boldsymbol{x} \in \Omega_{\mathrm{T}}} \left(T_{\theta_k}(\boldsymbol{x}) - \overline{T}_{\theta_k}\right)\left(P_{u,v}(\boldsymbol{x}) - \overline{P}_{u,v}\right)}{\sqrt{\sum_{\boldsymbol{x} \in \Omega_{\mathrm{T}}} \left(T_{\theta_k}(\boldsymbol{x}) - \overline{T}_{\theta_k}\right)^2} \sqrt{\sum_{\boldsymbol{x} \in \Omega_{\mathrm{T}}} \left(P_{u,v}(\boldsymbol{x}) - \overline{P}_{u,v}\right)^2}} \tag{24}$$

The NCC has values in the [−1, 1] range, where NCC = 1 indicates complete correspondence. By translating the template within the search window and evaluating the correlation at each position, an NCC response surface can be obtained. After repeating this process for different candidate rotation angles, the maximum NCC value is taken as the optimal registration result. Because this optimum lies on a discrete grid, the true NCC maximum usually lies between adjacent sampling points. Therefore, sub-pixel refinement is performed near the NCC maximum. Specifically, while using the discrete maximum as the center, bilinear interpolation is performed in the local neighborhood, and the peak position is re-estimated within a narrow search range [59]. Since the refinement is performed on the super-resolved image, the physical scale that is represented by each sub-pixel is further reduced, thereby improving the registration accuracy.

4. *In-situ* microscopic vision system

4.1. Hardware architecture

To obtain on-machine 3-DOF positioning measurements, a compact microscopic vision hardware system was incorporated into an ultra-precision lathe, as shown in Fig. 7. The system comprised a microscope objective, a coaxial illumination source, an industrial camera, and a displacement platform. These components were rigidly assembled as a unified module and then mounted on the tool-post base. As a result, pose deviations that were obtained from the image registration could be reliably mapped to displacement-compensation commands. The optical axis was aligned such that it was normal to the workpiece surface and its focus was adjusted using the machine motion axes. Therefore, it facilitated repeated observation of the same region during the machining, removal, and re-clamping cycles.

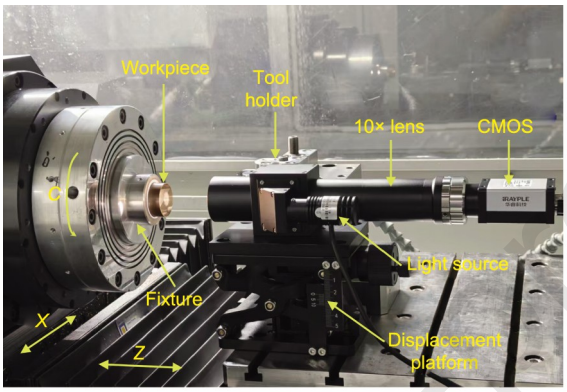

Fig. 7. On-machine microscopic vision hardware system.

A 10× telecentric microscope objective, which can provide an optical resolution of approximately 1.4 μm, was used to achieve reliable capture of fine microstructure textures. A depth of field of 10 μm, which can cover the depth variations of most ultra-precision microstructures while effectively avoiding defocus issues, was utilized. Meanwhile, an object-side working distance of 50 mm ensured that the compact system configuration had sufficient clearance to prevent interference with the machining process. The illumination module used a white-light coaxial source with adjustable brightness to reduce the reflectance variations and shadowing effects that were caused by changes in the incident angle. Thereby, illumination uniformity and photometric stability could be enhanced on the microstructure surfaces, and the sensitivities of intensity-dependent algorithms to illumination disturbances could be reduced. The industrial camera was equipped with a monochrome CMOS image sensor that had a resolution of 5120 × 5120 pixels and a pixel size of 2.5 μm. At a magnification of 10×, the system provided a field of view of approximately 1.28 mm × 1.28 mm, which corresponded to an object-space sampling interval of approximately 0.25 μm·pixel^{-1}. The ultra-precision lathe was equipped with an air-bearing vibration isolation platform and a granite base. All the machining and measurement experiments were conducted in a temperature-controlled environment that was maintained at (20 ± 1) °C. Consequently, the effects of environmental disturbances were effectively suppressed.

4.2. Imaging system performance

To satisfy the accuracy and robustness requirements of re-clamping positioning measurements during ultra-precision machining operations, the developed microscopic imaging system must provide reliable scale traceability and stable imaging performance. Therefore, a quantitative evaluation of the imaging system was conducted.

Firstly, pixel-size calibration was performed. A standardized USAF-1951 resolution test target was used as the calibration target. Fig. 8(a) depicts a local image of the target that was acquired by the developed microscopic imaging system. This image shows multiple groups of rectangular patterns with standard dimensions. Fig. 8(b) presents the correspondence between the pixel span across the bar-pattern cross-section and its nominal geometric length. Using this relationship, the pixel-size calibration coefficient, λ, was determined to be 0.248866 μm·pixel^{-1}.

Journal Pre-proofs

Secondly, to verify the stability and inter-frame consistency of the system under practical machining conditions, a stability test was conducted. While the workpiece was kept stationary and the imaging parameters remained unchanged, 300 consecutive microstructure images of the workpiece surface were captured in an actual machining environment. The structural similarity index measure (SSIM) and peak signal-to-noise ratio (PSNR) between different frames were then computed, as shown in Fig. 8(c). The results show that the SSIM remained within a range of 0.88377–0.88477, while the PSNR remained within a range of 38.31108–38.42669 dB, indicating stable frame-to-frame consistency. These outcomes suggest that environmental disturbances and readout noise imposed limited effects on the intensity field. Consequently, this system can provide a reliable imaging basis for subsequent 3-DOF positioning measurements.

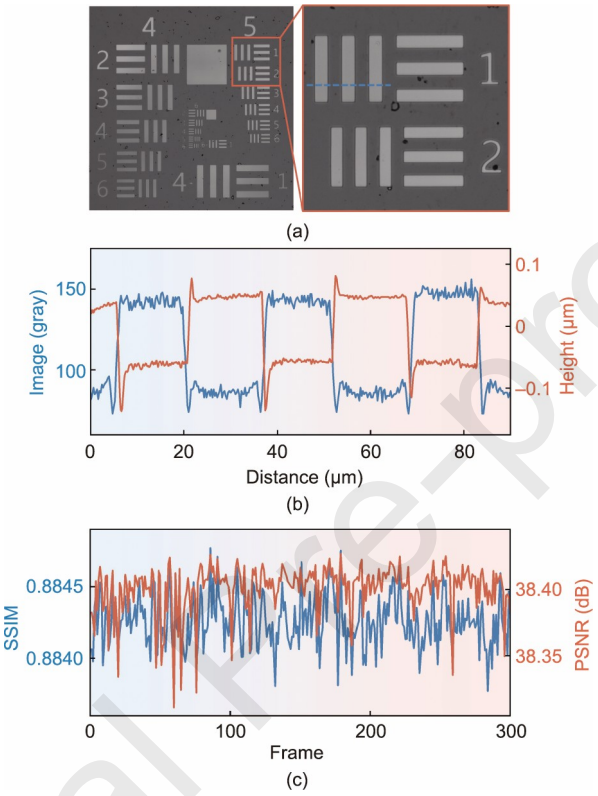

Fig. 8. Pixel size calibration and stability test of imaging system. (a) Microscopic optical image of a local region of the USAF-1951 resolution test chart; (b) correspondence between pixels and surface profile along a cross-section of the test chart; (c) consistency test results of adjacent frames in imaging stability experiment.

5. Experiments and results

5.1. Ultra-precision machining setup

During this study, micro features were fabricated on a three-axis ultra-precision lathe and were used as the target objects for re-clamping positioning measurements. The goal of this procedure was to verify the applicability and effectiveness of the proposed super-resolution microscopic vision-based 3-DOF positioning method under practical machining conditions. The machining system and the experimental setup are depicted in Fig. 9(a). The workpiece material was TU2 oxygen-free copper, which is commonly used in ultra-precision machining applications. To reduce the influence of the initial surface topography on the microstructure formation and the microscopic imaging, the end face of the workpiece was pre-processed by finish cutting with a large-radius circular-arc diamond tool. This process produced a smooth reference surface.

Subsequently, microstructures were machined on the end face according to the layout shown in Fig. 9(b). The microstructure pattern was composed of multiple intersecting straight microgrooves and circular-arc microgrooves. These features are representative of functional microstructure surfaces, such as gratings, reflective mirror-array microstructures, and microfluidic channels, which are

Journal Pre-proofs

frequently encountered in ultra-precision manufacturing operations. Groove depths of 3, 4, and 5 μm were utilized, and the cutting speed was 50 mm·min^{-1}. Two natural single-crystal diamond turning tools with identical specifications were used to machine the straight grooves and the circular-arc grooves. Each tool had a nose radius of 0.1 mm, a rake angle of 0°, and a clearance angle of 10°.

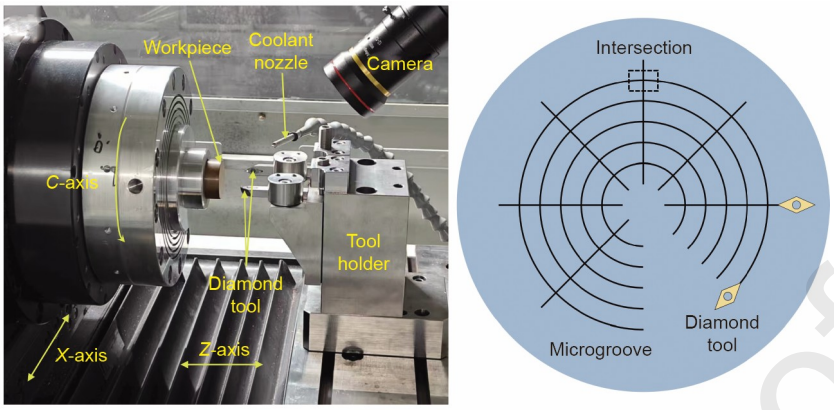

Fig. 9. Experimental ultra-precision machining of microstructures. (a) Diamond turning experiment setup; (b) schematic of the microstructure target.

5.2. Coarse positioning experiments and results

To evaluate the effectiveness and robustness of the proposed geometric-constraint-based 3-DOF coarse positioning algorithm, experiments were conducted over wide ranges of in-plane rotations and translations, and the resulting errors were statistically analyzed. Because the coarse positioning stage is intended to provide a reliable initialization for the fine positioning stage, the evaluation emphasized repeatability across a large search range, linearity, and the presence of systematic drift. The experiments were conducted on a three-axis ultra-precision lathe. The microstructure workpiece was mounted on the spindle face using a vacuum chuck, and prescribed in-plane motions were generated by the machine axes. Unavoidable motion errors exist during machine motion, and both axis errors and vibration can affect the positioning-measurement results. The steady-state error associated with the linear axes of the ultra-precision machine was within ±2 nm, and the positioning accuracy of the *C*-axis was less than 2″. To reduce the effects of the servo tracking error, the acceleration–deceleration transition error, and the dynamic vibrations, all the experiments were conducted at low speeds (with a translational speed of 1 mm·min^{-1} and a rotational speed of 10 (°)·min^{-1}). Image acquisition was performed only after the axes had stopped moving and the grating readings had stabilized. In addition, the environmental vibration was minimized as much as possible during the measurements. Therefore, the steady-state machine displacement was used as the reference value during this study, and the associated uncertainty was primarily bounded by the steady-state error range of the machine.

Fig. 10 presents the measurement results and error statistics for various reference value conditions. In these results, the error is defined as the difference between the measured value and the reference value. Firstly, in the rotational positioning experiment, the machine operated in the *C*-axis mode so that the workpiece was subjected to in-plane rotation. The rotation step was set to 1°, and the total rotation range was 180°. A microstructure image was captured at each angular position, and the orientation angle of the centerline of the straight groove was computed as the measurement. As shown in Fig. 10(a), the measured values followed the reference values very consistently within the −90° to 90° range, with a maximum error of 31.276″. Fig. 10(b) presents a histogram of the angular measurement errors together with the corresponding Gaussian fitting curve. The fitted peak center had a value of −0.952″ and a standard error of 0.985″.

During the translational test, unidirectional displacements of 0–180 μm with a step of 1 μm were set up along the *X* and *Y* axes. As shown in Figs. 10(c) and (e), the measured translations remained highly consistent with the reference values across the full stroke, and there was no observable error accumulation as the displacement increased. The maximum errors along the *X* and *Y* axes were −33.239 and −25.061 nm, respectively. Figs. 10(d) and (f) further present the corresponding error histograms and Gaussian fitting curves. The positioning error in the *X*-direction had a fitted peak center

Journal Pre-proofs

of 1.209 nm with a standard error of 0.812 nm, while the positioning error in the *Y*-direction had a fitted peak center of 1.907 nm with a standard error of 0.522 nm. The difference between the errors of the two directions was reasonable, and it was primarily attributed to directional variations in the microstructure texture and the sampling characteristics of the imaging system.

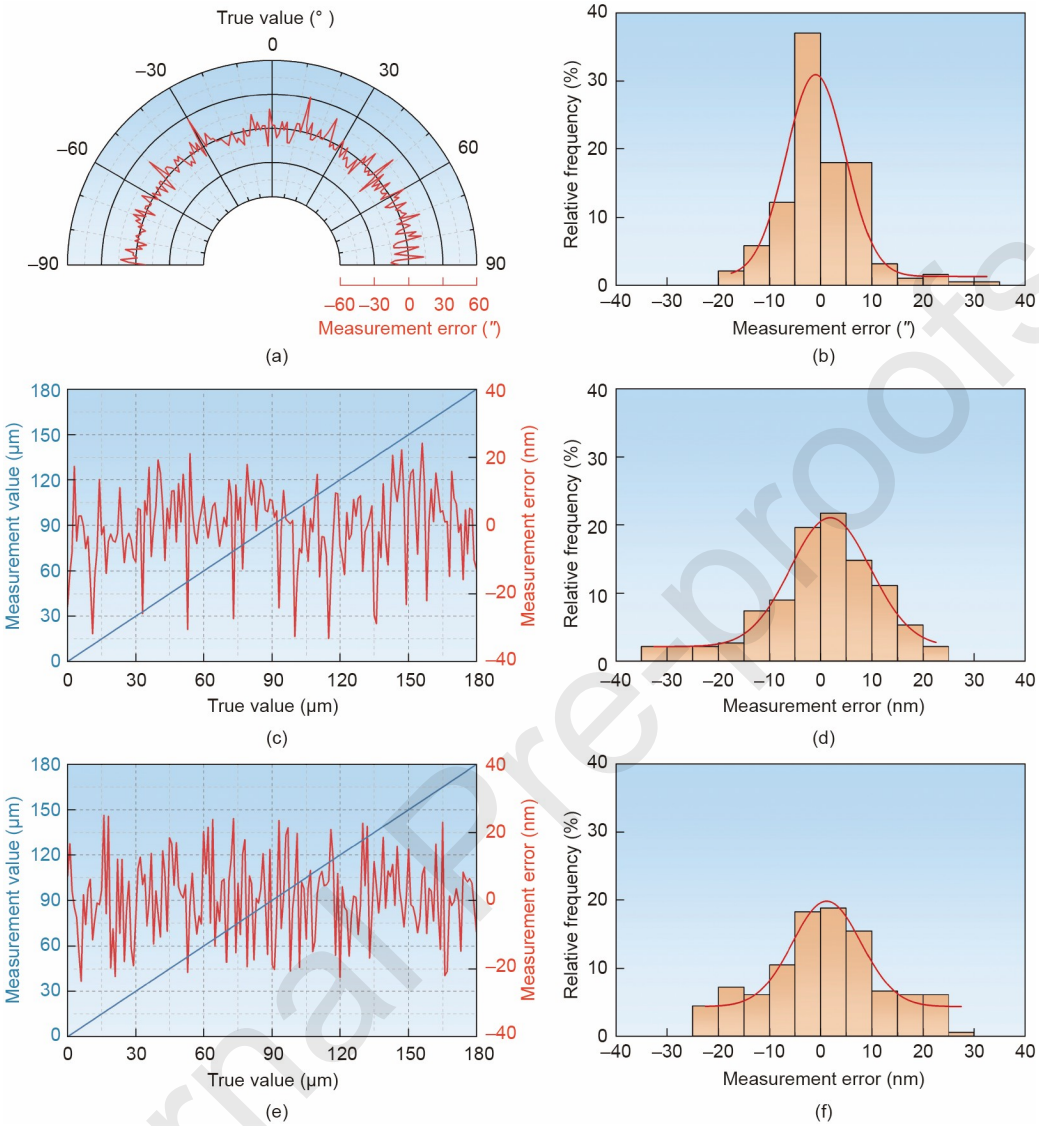

Fig. 10. Measurement results and error distributions of the coarse positioning stage based on geometric constraints. (a) Angular measurement results within a ±90° rotation range; (b) histogram and fitted distribution of the corresponding angular measurement errors; (c) translational measurement results along the *X*-axis within a 0–180 μm range; (d) histogram and fitted distribution of the corresponding measurement errors in the *X* direction; (e) translational measurement results along the *Y*-axis within a 0–180 μm range; (f) histogram and fitted distribution of the corresponding measurement errors in the *Y* direction.

Overall, the geometric-constraint-based coarse positioning method provided stable 3-DOF initial pose estimates over a large rotation range (180°) and a wide translation stroke (180 μm), and it exhibited concentrated errors and no evident systematic drift. Although this method was intended for initialization, the achieved accuracy (angular errors within ±40″ and translational errors within ±40 nm) was sufficient to constrain the subsequent fine-search space. Consequently, the efficiency and robustness of the overall coarse-to-fine positioning procedure were improved.

5.3. Super-resolution reconstruction experiments and results

Reconstruction experiments were conducted to evaluate the accuracy and robustness of the LIIF-

Journal Pre-proofs

based super-resolution model for the microscopic images of the machined microstructures. The super-resolution model was implemented in Python 3.8 with PyTorch 1.9.1 and CUDA 11.1.1, and it was trained on a single NVIDIA GeForce RTX 3090 GPU (NVIDIA, USA). The training was conducted for 1000 epochs using Adam with an initial learning rate of 1×10^{-4} and a MultiStepLR schedule. Test images were selected from the established microstructure dataset while being excluded from the training set to ensure objective evaluation. Bicubic interpolation was used as the baseline, and its results were compared with the results of representative single scale deep models, enhanced deep residual network (EDSR) [60] and RDN, and their meta-super-resolution (MetaSR) [61] variants, as well as with the LIIF based implementations, EDSR-LIIF and RDN-LIIF. Evaluations were conducted at scale factors of 2×, 4×, and 8×, and the reconstruction quality was quantified using the PSNR and the SSIM. Fig. 11 presents the PSNR and SSIM distribution statistics for the various algorithms across the tested scales. Overall, the LIIF family of models achieved better and more stable reconstruction at all the scales. Their advantages become more evident under higher magnifications, such as 4× and 8×, for which reconstruction is more challenging.

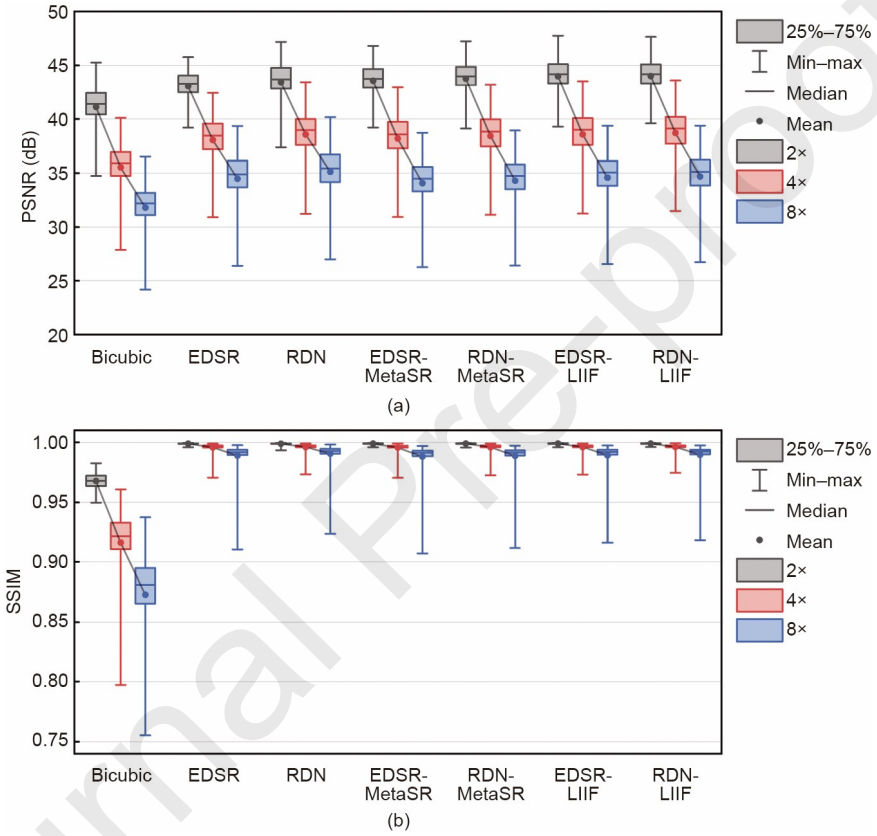

Fig. 11. Performance comparison of different super-resolution algorithms on microscopic microstructure images. (a) PSNR distributions at 2×, 4×, and 8× scale factors; (b) SSIM distributions at 2×, 4×, and 8× scale factors.

For the 2× scenario, all the learning based methods achieved high accuracies, with PSNR values that were typically above 40 dB and SSIM values that were greater than 0.96. These results indicate that the reconstruction task was relatively easy at this scale. As the scale factor increased, the reconstruction became more difficult and the performance disparities between the methods became more pronounced. The bicubic interpolation method exhibited a clear loss of fine details, as well as structural degradation. Among learning based methods, the performance reductions of the EDSR model and the MetaSR variants were more apparent. They were reflected by lower mean and median values and increased dispersion in the box plots. When the PSNR and SSIM were considered simultaneously, the RDN-LIIF model provided the most favorable balance for the microscopic microstructure reconstruction. Its PSNR and SSIM values remained optimal or nearly optimal across the 2×, 4×, and 8× scales with consistently small dispersion. It exhibited reliable performance for a variety of microstructure textures and imaging conditions. In addition, the implicit formulation of the LIIF method supports arbitrary scale reconstruction, which is beneficial for the proposed super-

resolution microscopic vision framework that requires flexible magnification.

To evaluate the detail recovery capability and reconstruction reliability of the adopted RDN-LIIF super-resolution method when used for microscopic images of microstructures, an 8× super-resolution reconstruction experiment was conducted using intersecting microgroove images. The spatial distribution of the reconstruction errors was visualized and analyzed. Specifically, a high-resolution image that was acquired by a laser confocal microscope was taken as the reference image. It was down-sampled by a scale factor of 8 to generate a corresponding low-resolution image, which was then reconstructed by the RDN-LIIF method at the same scale factor to obtain a super-resolved image.

Fig. 12 presents the reconstruction error as difference images, in which each pixel denotes the difference between the absolute grayscales of the reconstructed and reference images. Overall, the reconstruction errors had low magnitudes and a sparse spatial distribution. The differences were primarily concentrated in a few localized regions, while the large background areas showed near-zero errors. This result indicates that the low-frequency structures and most of the mid-frequency textures were faithfully recovered without any noticeable global intensity bias or structural distortion. Regions 1 and 2, which corresponded to the mirror-flat area and the groove interior, respectively, exhibited minimal deviations. This result confirmed that the intensity-field consistency was good in smoothly varying or quasi-uniform areas. In contrast, Region 3 was located at the intersection of the microstructure boundaries, where more pronounced error responses appeared in high-gradient neighborhoods, such as groove edges and micro-defects. These error responses reflect the inherent difficulty of recovering sharp edge details at high scale factors. These differences were confined to narrow boundary bands, and the peak error occupied only a small fraction of the dynamic grayscale range. Because the subsequent fine positioning relies on intensity consistency, the high grayscale fidelity that was observed across most of the regions indicates that 8× RDN-LIIF reconstruction can increase the effective resolution while maintaining the stability of intensity-based template matching refinement.

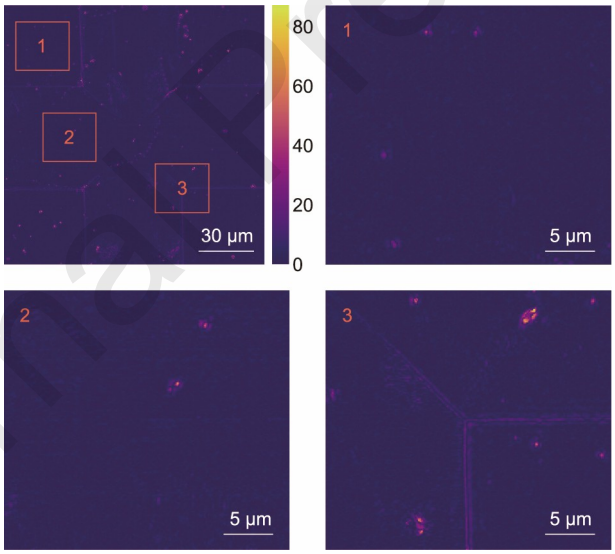

Fig. 12. Difference image of an intersecting microgroove reconstructed using the RDN-LIIF super-resolution method with 8× scale factor.

To further verify the contribution of super-resolution reconstruction to image-registration accuracy during the fine positioning stage, an ablation experiment that was aligned with the registration task was conducted. In this experiment, the image registration error was directly used as the evaluation metric by which the effects of different image enhancement methods on the positioning accuracy were compared. To avoid interference from the intrinsic motion errors of the machine tool, the workpiece was fixed on the spindle and kept stationary throughout the experiment, while microscopic images of the microstructure were continuously acquired. The intersecting microgroove region was selected as the test object, and the original images were cropped to 256 × 256 pixels, with a pixel size of 0.248866 $\mu m \cdot pixel^{-1}$. On this basis, five groups of input images were constructed for a template matching comparison: the original images, 2× bicubic interpolation images, 4× bicubic interpolation images, 8×

Journal Pre-proofs

bicubic interpolation images, and 8× RDN-LIIF super-resolution images. A 2D template matching method was adopted for the registration, and the NCC was used as the similarity metric. The template size was set to 70% of the global image. It should be noted that only the integer-pixel NCC peak, without sub-pixel interpolation refinement, was taken as the matching result in this experiment. Therefore, this experimental procedure was not identical to the fine positioning procedure that was described in Section 3.3.

Fig. 13 presents a comparison of the registration errors for various image enhancement conditions. For the original images, the mean registration error was 209.719 nm, the uncertainty was 12.693 nm, and the maximum error was 351.950 nm. After 2× bicubic interpolation was performed, the mean error decreased to 101.200 nm, with an uncertainty of 5.700 nm and a maximum error of 175.975 nm. When the interpolation factor was increased to 4×, the mean error was further reduced to 65.650 nm, with an uncertainty of 3.585 nm and a maximum error of 107.762 nm. For the 8× bicubic interpolation images, the mean error was 50.003 nm, the uncertainty was 2.553 nm, and the maximum error was 76.199 nm. In contrast, after 8× RDN-LIIF super-resolution reconstruction was performed, the mean error was further reduced to 27.942 nm, with an uncertainty of 1.710 nm and a maximum error of 53.881 nm. These results demonstrate that the registration error decreased continuously as the effective image resolution increased. Of these methods, the 8× RDN-LIIF super-resolution reconstruction approach yielded the lowest error. The result indicates that this method can effectively improve the image-registration accuracy.

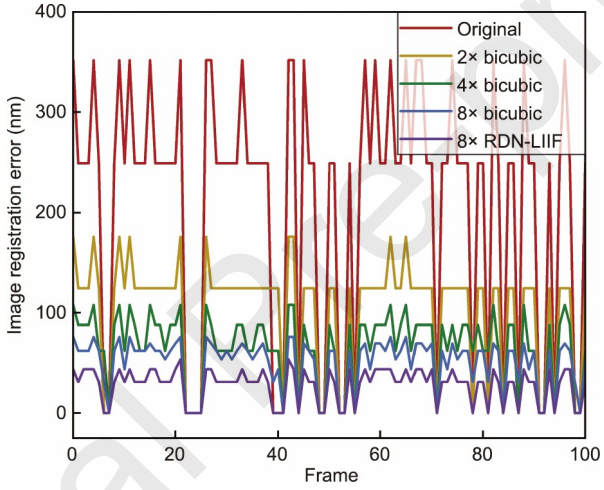

Fig. 13. Effect of super-resolution reconstruction on the improvement of image registration accuracy.

5.4. Fine positioning experiments and results

To validate the measurement accuracy of the template matching based fine positioning stage, a 3-DOF positioning experiment was conducted after super-resolution reconstruction was performed. In the experiment, the workpiece was kept stationary on the machine tool, while the microscopic imaging system acquired an image sequence of the same microstructure region at various time instants. The 3-DOF template matching procedure was then performed between different frames.

The first image was used as the reference, and a 256 × 256 pixels intersecting-groove region was selected for the registration. This region was then super-resolved by the 8× RDN-LIIF model, thereby increasing the image size from 256 × 256 pixels to 2048 × 2048 pixels, while the template size was cropped to 1800 × 1800 pixels. The effective pixel size after super-resolution was performed was 0.031108 μm·pixel^{-1}. Since coarse positioning had already constrained the residual rotation to within ±40″, the rotation search in the fine positioning stage was set to [−60″, 60″] with a 3″ step. For translation, because the linear-axis error from the coarse positioning stage was within ±40 nm and because residual rotation may induce translation coupling at the template scale, a translation window with a size of 20 pixels, which corresponded to approximately 0.625 μm × 0.625 μm, was used on the super-resolved image. This setting covered the residual errors while avoiding the computational cost of a global 3-DOF search.

Journal Pre-proofs

Fig. 14 presents the 3-DOF positioning results and error distribution for the fine positioning stage. Fig. 14(a) depicts the angular measurement errors for the fine positioning stage. The mean rotational error was 0.094″, with an uncertainty of 0.028″, while the maximum error was −11.583″. Fig. 14(b) presents a histogram of the angular measurement errors along with the corresponding Gaussian fitting curve. The fitted peak center was 0.309″, with a standard error of 0.437″. Fig. 14(c) shows the translational measurement errors along the *X*-axis for the fine positioning stage. The mean *X*-direction error was 0.226 nm, with an uncertainty of 0.042 nm, while the maximum error was −18.534 nm. Fig. 14(d) presents a histogram of the *X*-direction translational measurement errors along with the corresponding Gaussian fitting curve. The fitted peak center was 0.359 nm, with a standard error of 0.741 nm. Fig. 14(e) presents the translational measurement errors along the *Y*-axis for the fine positioning stage. The mean *Y*-direction error was 0.871 nm, with an uncertainty of 0.040 nm, while the maximum error was −17.910 nm. Fig. 14(f) shows a histogram of the *Y*-direction translational measurement errors along with the corresponding Gaussian fitting curve. The fitted peak center was 1.096 nm, with a standard error of 0.621 nm. These results demonstrate that, benefiting from the combination of super-resolution enhancement and small-range 3-DOF template matching, the fine positioning stage can achieve arcsecond-level rotation estimations and translation measurements on the scale of tens of nanometers.

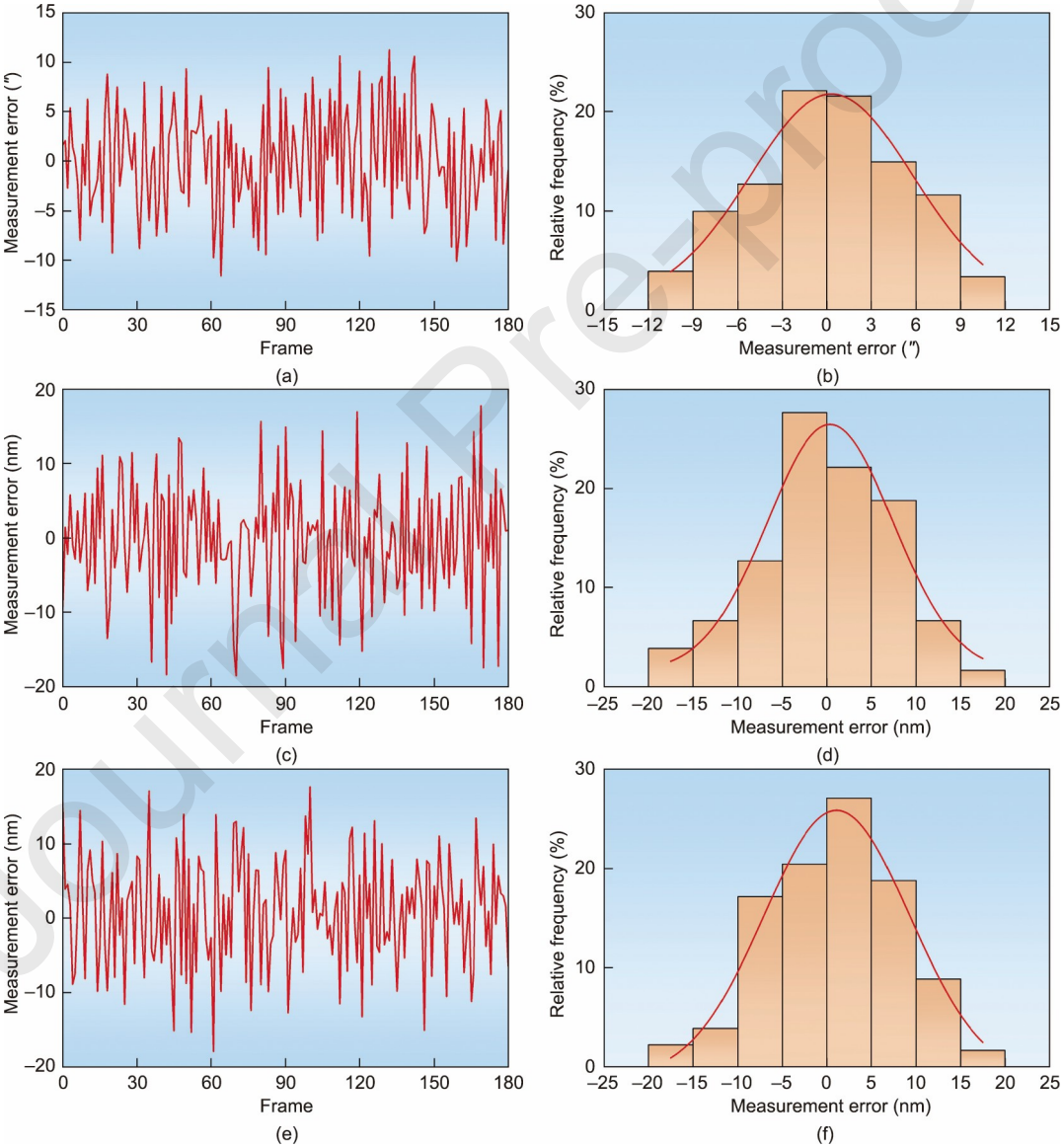

Fig. 14. Measurement results and error distributions of the fine positioning stage based on 3-DOF template matching. (a) Measurement results in-plane rotation in different frames; (b) histogram and fitted distribution of the corresponding angular errors; (c) measurement results translation along the *X*-axis in different frames; (d) histogram and fitted distribution of the corresponding *X*-axis errors; (e)

Journal Pre-proofs
measurement results translation along the *Y*-axis in different frames; (*f*) histogram and fitted distribution of the corresponding *Y*-axis errors.

5.5. Verification experiments for the positioning system

Verification experiments were conducted for the complete workflow that was developed during this study, which follows the sequence "reference image acquisition–workpiece motion–current image acquisition–coarse positioning–super-resolution reconstruction–fine positioning." Unlike the validation experiments for the individual algorithmic modules, these experiments were focused on the complete measurement chain with the goal of evaluating the overall effectiveness of the proposed positioning measurement system at the system level for practical applications.

In the experiments, the workpiece was fixed on the spindle and separately subjected to a rotation of 3° and a translation of 30 μm. Next, measurement was performed using the complete workflow. During the coarse positioning stage, the image size was 1000 × 1000 pixels, with a pixel size of 0.248866 $\mu m \cdot pixel^{-1}$. During the super-resolution reconstruction stage, the RDN-LIIF model was employed for 8× reconstruction. During the fine positioning stage, the super-resolved image size was 2048 × 2048 pixels, which corresponded to an original image size of 256 × 256 pixels, with a pixel size of 0.031108 $\mu m \cdot pixel^{-1}$. The rotational search range for the template matching process was set to [−60″, 60″] with a step of 3″, and the translational search window was set to 20 pixels.

Fig. 15 presents the measurement results and error distributions for the positioning system over 100 repeated experiments. Fig. 15(a) presents the rotational measurement results, which exhibited a mean measurement error of −0.823″, an uncertainty of 0.789″, and a maximum error of −19.219″. Fig. 15(b) depicts a histogram of the rotational measurement errors and the corresponding Gaussian fitting result, for which the fitted peak center was −0.111″ and the standard error was 0.399″. Fig. 15(c) shows the translational measurement results, which had a mean measurement error of 0.941 nm, an uncertainty of 0.978 nm, and a maximum error of −24.875 nm. Fig. 15(d) presents a histogram of the translational measurement errors and the corresponding Gaussian fitting result, for which the fitted peak center was 1.174 nm and the standard error was 0.636 nm. In addition, for this experimental setup, the computation time for one measurement was less than 30 s. This time corresponds to the complete workflow, which includes image acquisition, coarse positioning, super-resolution reconstruction, and fine positioning. In consideration of both the measurement accuracy and the time cost, the proposed system demonstrated good engineering feasibility for re-clamping positioning during ultra-precision machining operations.

Journal Pre-proofs

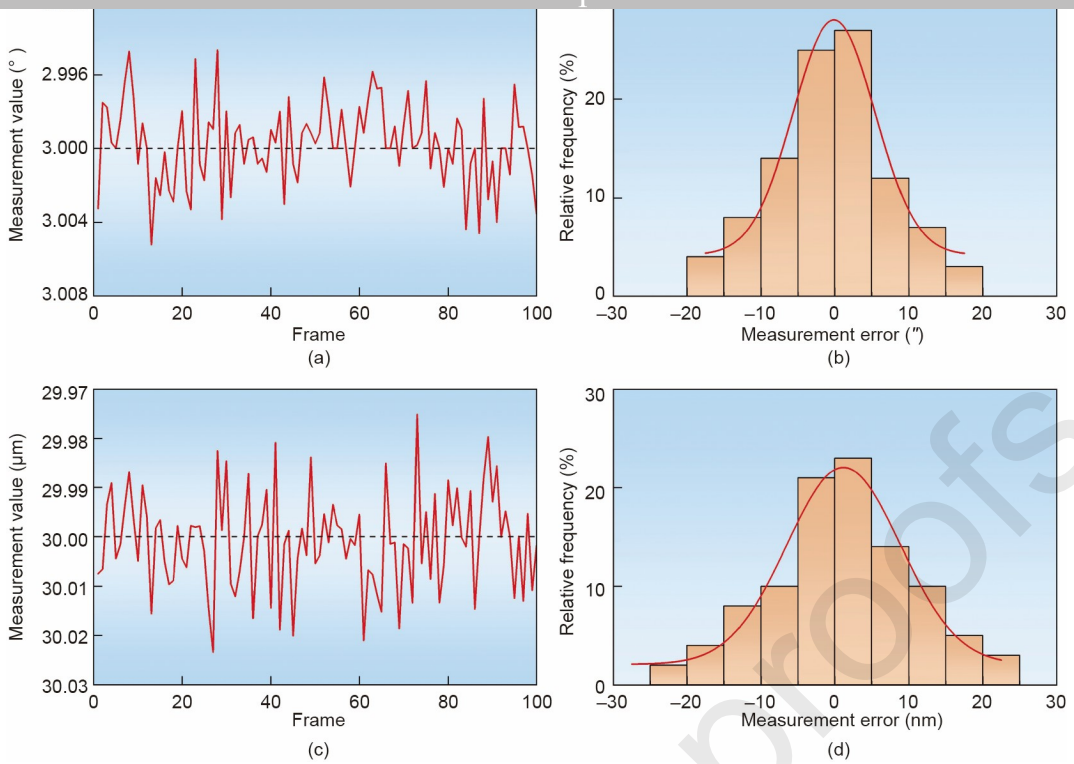

Fig. 15. Measurement results and error distributions of the positioning system. (a) Rotational measurement results; (b) histogram and fitted distribution of the rotational errors; (c) translational measurement results; (d) histogram and fitted distribution of the translational errors.

6. Conclusions

This paper proposes a super-resolution microscopic vision-based 3-DOF positioning system for the accurate measurement of re-clamping errors during ultra-precision machining operations. This framework includes on-machine microscopic imaging, microstructure-oriented deep learning super-resolution reconstruction, and a hierarchical coarse-to-fine image registration strategy. The proposed system uses two images, one of which is acquired before and the other of which is acquired after re-clamping, to estimate the relative in-plane translation and rotation of the workpiece. By treating the machined microstructures as intrinsic references, this method avoids auxiliary fiducials and provides a direct basis for high-precision workpiece repositioning.

An on-machine microscopic imaging module was developed and integrated into the ultra-precision machining platform. A coarse-to-fine registration pipeline was established to jointly address the requirements of a large capture range and a high positioning accuracy. During the coarse positioning stage, repeatable geometric primitives that are extracted from microstructure edges are used for geometry-constrained initialization. Sub-pixel edge refinement and geometric fitting yield a reliable initial pose estimate even when large displacements and partial overlap are present. To address the difficulties associated with super-resolution reconstruction at the microscopic scale, a dedicated high-resolution microstructure dataset was constructed using laser confocal microscopy. In addition, an RDN-LIIF network was trained to achieve continuous-scale super-resolution reconstruction, thereby improving the registration accuracy. The super-resolved images are then used in the fine positioning stage, where 3-DOF sub-pixel template matching that is based on NCC is used to refine the residual pose deviation within the constrained neighborhood.

Systematic experiments were performed to validate the proposed system at both the module and system levels. During the coarse positioning stage, the proposed method constrained the error within ±40″ and ±40 nm over a rotation range of 180° and a translation range of 180 μm. Using the customized microstructure dataset, the RDN-LIIF model achieved a better reconstruction quality than other methods and effectively improved the image resolution and registration accuracy over scaling factors that ranged from 2× to 8×. During the fine positioning stage, the combination of super-resolution

Journal Pre-proofs

enhancement and small-range 3-DOF template matching achieved arcsecond-level rotation estimations and nanometer-level mean translational measurement errors, with maximum deviations that were on the scale of tens of nanometers. Furthermore, system-level validation experiments demonstrated that the proposed positioning system can achieve rotational measurement errors below 20″ and translational measurement errors below 25 nm.

Overall, the proposed vision-based positioning system provides a non-contact and cost-effective solution for re-clamping error measurement, and it is directly compatible with practical ultra-precision machining workflows. At present, the method is primarily applicable to microstructure surfaces with repeatable intrinsic patterns that support robust registration. It cannot yet be directly extended to feature-sparse surfaces, such as complex specular mirrors. Future work will extend the framework toward higher-degree-of-freedom positioning and broader precision alignment scenarios while further improving its robustness in the presence of more challenging operating conditions.

Acknowledgements

The authors would like to acknowledge the financial support from the National Key Research and Development Program of China (2023YFB3407300, 2025YFE0203200). This work was also supported by grants from the National Natural Science Foundation of China [52522509, 52175420], Natural Science Foundation of Shandong Province (ZR2024ZD43), and the Self-developed Instrument and Equipment Project of Shandong University (zy20240303).

References

[1] Zhang ZY, Yan JW, Kuriyagawa T. Manufacturing technologies toward extreme precision. Int J Extreme Manuf 2019;1(2):022001.

[2] He GW, Huang QQ, Li XH, Zhou LB, Yang M, Luo YD, et al. AI-powered semiconductor wafer fabrication: a manufacturing paradigm shift. Int J Mach Tools Manuf 2026;214:104345.

[3] Xue B, Yan HL, Liu ZC, Yan YD, Geng YQ. Achieving tip-based down-milling forming of nanograting structures with variable heights through precise control of nano revolving trajectories. Int J Extreme Manuf 2025;7(5):055101.

[4] Zhao L, Zhang JJ, Zhang JG, Dai HF, Hartmaier A, Sun T. Numerical simulation of materials-oriented ultra-precision diamond cutting: review and outlook. Int J Extreme Manuf 2023;5(2):022001.

[5] Zhang SJ, Zhou YP, Zhang HJ, Xiong ZW, To S. Advances in ultra-precision machining of micro-structured functional surfaces and their typical applications. Int J Mach Tools Manuf 2019;142:16–41.

[6] Lai T, Liu JF, Chen FL, Li ZL, Guan CL, Li H, et al. Allocation of geometrical errors for developing precision measurement machine. J Intell Manuf 2025;36(6):4105–27.

[7] Gao W, Ibaraki S, Donmez MA, Kono D, Mayer JRR, Chen YL, et al. Machine tool calibration: measurement, modeling, and compensation of machine tool errors. Int J Mach Tools Manuf 2023;187:104017.

[8] Luo XC, Liu Q, Madathil AP, Xie WK, Rowe WB. Predictive digital twin-driven dynamic error control for slow-tool-servo ultraprecision diamond turning. CIRP Ann 2024;73(1):377–80.

[9] Yu J, Shen Z, Wang X, Sheng P, Wang Z. *In situ* noncontact measurement system and two-step compensation strategy for ultra-precision diamond machining. Opt Express 2018;26(23):30724–39.

[10] Wang P, Qu H, Zhang QL, Xu X, Yang S. Production quality prediction of multistage manufacturing systems using multi-task joint deep learning. J Manuf Syst 2023;70:48–68.

[11] Magnanini MC, Demir O, Colledani M, Tolio T. Performance evaluation of multi-stage manufacturing systems operating under feedback and feedforward quality control loops. CIRP Ann 2024;73(1):349–52.

[12] Xing TJ, Zhao XS, Song LQ, Cui ZP, Zou XC, Sun T. On-machine measurement method and geometrical error analysis in a multi-step processing system of an ultra-precision complex spherical surface. J Manuf Process 2022;80:161–77.

[13] Luo X. High-precision fabrication of 4m SiC aspheric mirror. Light Sci Appl 2023;12(1):4.

[14] Wang S, Kong L, Wang C, Cheung C. Ultra-precision manufacturing of microlens arrays using an optimum machining process chain. Opt Express 2023;31(2):2234–47.

Journal Pre-proofs

[15] Chen ZQ, Yu Q, Shimada K, Liu Y, He YY, Hu Y, et al. High-precision and high-efficiency fabrication of blazed grating by ultrasonic-assisted ultraprecision planing. J Mater Process Technol 2023;311:117802.

[16] Modarelli MJC, Kot-Thompson DM, Hoshino K. 5-Axis CNC micro-milling machine for three-dimensional microfluidics. Lab Chip 2025;25(2):127–42.

[17] Wang S, Zhao QL. Development of an on-machine measurement system with chromatic confocal probe for measuring the profile error of off-axis biconical free-form optics in ultra-precision grinding. Measurement 2022;202:111825.

[18] Geng ZC, Tong Z, Jiang XQ. Review of geometric error measurement and compensation techniques of ultra-precision machine tools. Light Adv. Manuf. 2021;2(2):211.

[19] Yu YQ, Wang ZY, Zhang SZ, Ren MJ, Zhu LM, Zhang XQ. Toolpath smoothing and motion planning for the diamond turning of microlens arrays with improved uniformity. Precis Eng 2025;95:350–63.

[20] Kumar S, Tong Z, Jiang XQ. Advances in the design and manufacturing of novel freeform optics. Int J Extreme Manuf 2022;4(3):032004.

[21] Zeng Z, Zhou T, Yu Q, Zhou J, Wang G, Xie Q, et al. Alignment error modeling and control of a double-sided microlens array during precision glass molding. Microsyst Nanoeng 2024;10(1):48.

[22] Wang JQ, Zhu WH, Yan YD, Verma J, Zhao XS, Geng YQ. Modelling and experimental study of nanomilling 3D nanogrooves on GaSb surfaces. Int J Extreme Manuf 2026;8(3):035101.

[23] Möhring HC, Biermann D, Bleicher F, Melkote S, Kappmeyer G. Fixtures and workpiece clamping systems in machining. CIRP Ann 2025;74(2):945–69.

[24] Wang Y, Dong ZG, Tian JC, Bao Y, Kang RK, Qin Y. Deformation prediction of circular cell honeycomb under fixture-workpiece systems. Int J Mech Sci 2025;290:110120.

[25] Ben-Hanan U, Eckert U, Mende M, Weiss A, Wertheim R, Azaria U. Development of a pneumatic clamping system with position and force control machining. In: Proceedings of the 18th Global Conference on Sustainable Manufacturing-GCSM-Annual; 2022 Oct 5–7; Berlin, Germany. Cham: Springer Nature; 2022. p. 184–92.

[26] Wang SX, Cheung B, Ren MJ. Uncertainty analysis of a fiducial-aided calibration and positioning system for precision manufacturing of optical freeform optics. Meas Sci Technol 2020;31(6):065012.

[27] Egaña F, Yagüe-Fabra JA, Mutilba U, Vez S. Machine tool integrated inverse multilateration uncertainty assessment for the volumetric characterisation and the environmental thermal error study of large machine tools. CIRP Ann 2021;70(1):435–8.

[28] Sun ZW, Xu SJ, Jiao J, Wang SJ, To S, Li PZ. Surface deformation errors and self-adaptive compensation for microstructured surface generation of titanium alloys. Int J Mech Sci 2022;236:107736.

[29] Qin Y, Kang RK, Sun JS, Wang YD, Zhu XL, Dong ZG. A fast self-calibration method of line laser sensors for on-machine measurement of honeycomb cores. Opt Lasers Eng 2022;152:106981.

[30] Lang W, Zhang XC, Chen YN, Chen T, Yang PD, Xu M, et al. Deterministic form-position deflectometric measurement of monolithic multi-freeform optical structures via Bayesian multisensor fusion. Light Adv Manuf 2025;6(2):260.

[31] Chen T, Chen YN, Zhang XC, Wang W, Xu M. Workpiece positioning and error decoupling in the single-point diamond turning of freeform mirrors based on the monoscopic deflectometry. Precis Eng 2022;77:16–23.

[32] Gao W, Haitjema H, Fang FZ, Leach RK, Cheung CF, Savio E, et al. On-machine and in-process surface metrology for precision manufacturing. CIRP Ann 2019;68(2):843–66.

[33] Wang W, Liu W, Liu Y, Zhang Y, Jia Z. Precise 2D and 3D Hybrid measurement of drill bits with complex geometries. Engineering. In press.

[34] Gao YP, Li XY, Wang XV, Wang LH, Gao L. A Review on recent advances in vision-based defect recognition towards industrial intelligence. J Manuf Syst 2022;62:753–66.

[35] He WB, Jiang ZW, Ming WY, Zhang GJ, Yuan J, Yin L. A critical review for machining positioning based on computer vision. Measurement 2021;184:109973.

[36] Wang X, Jian ZX, Wen DZ, Zhang XQ, Zhu LM, Ren MJ. Anisotropic neural reflectance model for measuring curved machined metal surface. IEEE Trans Industr Inform 2024;20(12):13547–58.

Journal Pre-proofs

[37] Jing JY, Liu S, Wang G, Zhang WCA, Sun CM. Recent advances on image edge detection: a comprehensive review. Neurocomputing 2022;503:259–71.

[38] Li HL, Fang XM, Zhu ZJ, Fu WP, Zhao CY. The approach of nanoscale vision-based measurement via diamond-machined surface topography. Measurement 2023;214:112814.

[39] Qiao C, Li D, Guo YT, Liu C, Jiang T, Dai QH, et al. Evaluation and development of deep neural networks for image super-resolution in optical microscopy. Nat Methods 2021;18:194.

[40] Zhan HY, Xing F, Bao JY, Sun T, Chen ZZ, You Z, et al. Analyzing the effect of the intra-pixel position of small PSFs for optimizing the PL of optical subpixel localization. Engineering 2023;27:140–9.

[41] Zuo C, Qian J, Feng S, Yin W, Li Y, Fan P, et al. Deep learning in optical metrology: a review. Light Sci Appl 2022;11(1):39.

[42] Ma JY, Jiang XY, Fan AX, Jiang JJ, Yan JC. Image matching from handcrafted to deep features: a survey. Int J Comput Vis 2021;129(1):23–79.

[43] Xu H, Yuan J, Ma J. MURF: mutually reinforcing multi-modal image registration and fusion. IEEE Trans Pattern Anal Mach Intell 2023;45(10):12148–66.

[44] Zhang YL, Tian YP, Kong Y, Zhong BN, Fu Y. Residual dense network for image super-resolution, In: Proceedings of the 31st IEEE/CVF Conference on Computer Vision and Pattern Recognition; 2018 Jun 18–22; Salt Lake City, UT, USA. New York City: IEEE; 2018. p. 2472–81.

[45] Chen YB, Liu SF, Wang XL, Ieee Comp SOC. Learning continuous image representation with local implicit image function. In: Proceedings of the IEEE/CVF Conference on Computer Vision and Pattern Recognition; 2021 Jun 19–25; held vitrually. New York City: IEEE; 2021. p. 8624–34.

[46] Pang SQ, Zhang XM, Li H, Lu YH. Edge determination improvement of scanning electron microscope images by inpainting and anisotropic diffusion for measurement and analysis of microstructures. Measurement 2021;176:109217.

[47] Wang ZQ, Peng YF, Fang L, Gao L. Computational optical imaging: on the convergence of physical and digital layers. Optica 2025;12(1):113–30.

[48] Xie X, Chen Y, Yang K, Zhou J. Harnessing the point-spread function for high-resolution far-field optical microscopy. Phys Rev Lett 2014;113(26):263901.

[49] Lin X, Zhou Y, Liu Y, Zhu C. A comprehensive review of image line segment detection and description: taxonomies, comparisons, and challenges. IEEE Trans Pattern Anal Mach Intell 2024;46(12):8074–93.

[50] Seo S. Subpixel edge localization based on adaptive weighting of gradients. IEEE Trans Image Process 2018;27(11):5501–13.

[51] Liu Z, Guan B, Shang Y, Yu Q, Kneip L. Line-based 6-DoF object pose estimation and tracking with an event camera. IEEE Trans Image Process 2024;33:4765–80.

[52] Lepcha DC, Goyal B, Dogra A, Goyal V. Image super-resolution: a comprehensive review, recent trends, challenges and applications. Inf Fusion 2023;91:230–60.

[53] Su H, Li Y, Xu YF, Fu X, Liu S. A review of deep-learning-based super-resolution: from methods to applications. Pattern Recognit 2025;157:110935.

[54] Chen HG, He XH, Qing LB, Wu YY, Ren C, Sheriff RE, et al. Real-world single image super-resolution: a brief review. Inf Fusion 2022;79:124–45.

[55] Jung J, Na J, Park HK, Park JM, Kim G, Lee S, et al. Super-resolving material microstructure image via deep learning for microstructure characterization and mechanical behavior analysis. npj Comput Mater 2021;7(1):96.

[56] Dong C, Loy CC, He K, Tang X. Image super-resolution using deep convolutional networks. IEEE Trans Pattern Anal Mach Intell 2016;38(2):295–307.

[57] Gao C, Feng A, Liu X, Taylor RH, Armand M, Unberath M. A fully differentiable framework for 2D/3D registration and the projective spatial transformers. IEEE Trans Med Imaging 2024;43(1):275–85.

[58] Gao ZR, Yi RJ, Qin Z, Ye YF, Zhu CY, Xu K. Learning accurate template matching with differentiable coarse-to-fine correspondence refinement. Comput Vis Media 2024;10(2):309–30.

Journal Pre-proofs

[59] Joseph EV, Laga H, Boussaid F, Bennamoun M. Generalized closed-form formulas for feature-based subpixel alignment in patch-based matching. Int J Comput Vis 2025;133(9):5958–75.

[60] Lim B, Son S, Kim H, Nah S, Lee KM. Ieee, Enhanced deep residual networks for single image super-resolution. In: Proceedings of the 30th IEEE/CVF Conference on Computer Vision and Pattern Recognition Workshops; 2017 Jul 21–26; Honolulu, HI, USA. New York City: IEEE; 2017. p. 1132–40.

[61] Hu XC, Mu HY, Zhang XY, Wang ZL, Tan TN, Sun J, et al. Meta-SR: a magnification-arbitrary network for super-resolution. In: Proceedings of the 32nd IEEE/CVF Conference on Computer Vision and Pattern Recognition; 2019 Jun 16–20; Long Beach, CA, USA. New York City: IEEE; 2019. p. 1575–84.

Declaration of Interest Statement

☒ The authors declare that they have no known competing financial interests or personal relationships that could have appeared to influence the work reported in this paper.

☐ The author is an Editorial Board Member/Editor-in-Chief/Associate Editor/Guest Editor for this journal and was not involved in the editorial review or the decision to publish this article.

☐ The authors declare the following financial interests/personal relationships which may be considered as potential competing interests:

Journal Pre-proofs